Microwatt Microwave (M^2) Oscillator: Going Beyond the Delegation Architecture of Low-power Wireless Communication

Pramuka Sooriya Patabandige*
National University of Singapore
pramuka@u.nus.edu

Dhairya Shah*
National University of Singapore
dhairya@u.nus.edu

Rajashekar Reddy Chinthalapani
National University of Singapore
rajashekar.c@u.nus.edu

Spanddhana Sara
National University of Singapore
spanddhanasara@u.nus.edu

Prabal Dutta
UC Berkeley
prabal@berkeley.edu

Ambuj Varshney
National University of Singapore
ambujv@nus.edu.sg

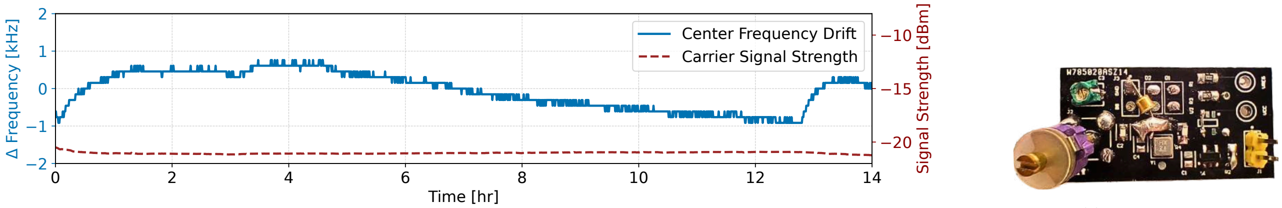

(a) Long-term frequency stability of M^2 over a period of 14 hours

(b) M^2 Prototype

Figure 1: M^2 generates microwave signals through an oscillator that breaks the stability-power tradeoff. By coupling a tunnel diode with a SAW resonator, M^2 achieves 2.10 ppm **stability at** 434.22 MHz **over** 14 hours**, with maximum drift of only** 916 Hz **under** 105 µW**. This is orders of magnitude below state-of-the-art tunnel diode oscillators and comparable to conventional oscillators consuming higher power. The carrier strength remains stable throughout the measurement.**

Abstract

For the past decade, low-power communication has relied on a *delegation architecture* that offloads carrier signal generation to external emitter devices. Although this reduces transmitter and receiver power, the resulting three-device topology introduces deployment complexity that has hindered wider adoption. Returning to a true two-device architecture on a microwatt budget was considered impossible because stable microwave oscillators are inherently power-hungry. We introduce M^2, which breaks the trade-off between stability and power. The key contribution is an oscillator that generates microwave signals below 105 µW while maintaining stability of a few ppm, achieved by coupling a tunnel diode with a high-Q SAW resonator. Over a multi-hour deployment, this stability is at least two orders of magnitude better than state-of-the-art tunnel diode oscillators and is maintained across controlled variations in temperature, humidity, and motion, as well as uncontrolled real-world conditions including a crowded university food court and outdoor environment with direct sun exposure. Furthermore, M^2 exhibits self-oscillating mixing and autodyning, enabling standalone transmitters and receivers that achieve 135 m line-of-sight range and −75 dBm reception sensitivity, with ranges exceeding tens of meters in tag-to-tag topology. M^2 takes a major step beyond the de facto delegation architecture, enabling a new class of stable, standalone *microwatt microwave (M^2)* radio transceivers.

CCS Concepts

• **Hardware → Sensor devices and platforms**; **Wireless devices**; *Networking hardware*; • **Computer systems organization → Sensor networks**.

Keywords

Embedded systems, Wireless transmitters, Receivers, Tunnel diodes

ACM Reference Format:
Pramuka Sooriya Patabandige, Dhairya Shah, Rajashekar Reddy Chinthalapani, Spanddhana Sara, Prabal Dutta, and Ambuj Varshney. 2026. Microwatt Microwave (M^2) Oscillator: Going Beyond the Delegation Architecture of Low-power Wireless Communication. In *The 24th Annual International Conference on Mobile Systems, Applications and Services (MobiSys '26), June 21–25, 2026, Cambridge, United Kingdom.* ACM, New York, NY, USA, 19 pages. https://doi.org/10.1145/3745756.3809248

1 Introduction

For the past quarter-century, embedded systems research has been driven by the power consumption of communication [2, 15, 20, 41, 42, 50, 91, 93, 97], creating deployment including logistical complexity, frequent battery replacements, and form-factor restrictions [4]. Early efforts addressed power-challenges with radio duty cycling [15, 97], suitable for small, infrequent packets. But as applications evolved towards continuous high-volume data transfer [63, 92], milliwatt transceiver power became unavoidable.

Transceiver power stems from analog components such as oscillators, mixers, and amplifiers for carrier generation and signal conditioning. While digital components have benefited from Moore's Law, analog counterparts have not seen comparable efficiency gains [42]. The predominant strategy, spanning backscatter transmitters [20, 42, 50, 91, 100, 120], injection-locked transmitters [60, 104], and receivers [58, 74, 78], is delegation, offloading tasks such as carrier generation to an emitter device (ED). This

---

*Co-primary authors with equal contributions to this work.

MobiSys '26, Cambridge, United Kingdom

ACM ISBN 979-8-4007-2027-7/2026/06
https://doi.org/10.1145/3745756.3809248

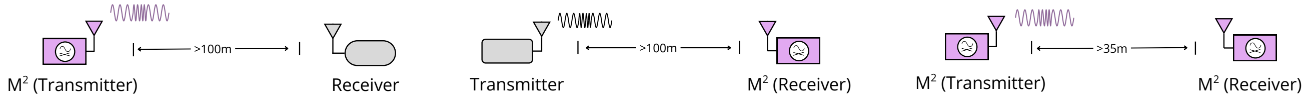

(a) Transmitter instantiated using M^2 (b) Receiver instantiated using M^2 (c) Tag-to-tag link using two M^2 transceivers

Figure 2: M^2 is a stable microwatt oscillator that enables two-device transmitter (a), receiver (b), and symmetric tag-to-tag (c) link without a dedicated ED.

has enabled low-power transmitters to support commodity standards [20, 38, 42, 71, 91, 118], achieve long range [70, 91, 100], and open new applications [4, 63, 92, 102].

Despite promising results suggesting the energy challenge is solved, real-world deployments still suffer from the delegation architecture. The three-device topology (transmitter, receiver, ED) introduces deployment complexity impractical for most scenarios, preventing technologies such as backscatter transmitters [20, 42] and Schottky-diode receivers [58, 74, 78] from widespread adoption.

The holy grail of embedded systems is a return to a true two-device architecture on a microwatt budget. This was considered impossible because generating a stable high-frequency carrier signal is inherently power-consuming [42, 50]. Phase-locked loops consume milliwatts, and microwatt alternatives such as tunnel diode oscillators (TDO) [65, 96, 99, 103, 104] lack the required stability for communication. We demonstrate M^2, a highly stable microwave oscillator under 105 µW instantiated for 433 MHz band.

Design. M^2 challenges the long-held notion that low power and frequency stability in an oscillator are fundamentally incompatible. It revisits oscillator design through the unique physics of tunnel diodes, semiconductor devices with a heavily doped p-n junction in which electrons tunnel quantum-mechanically through the barrier rather than overcoming it [21, 22], producing negative differential resistance (NDR) at low voltages and currents [81]. This enables microwatt power for microwave operation up to several GHz.

Recent years have seen renewed interest in tunnel diodes for embedded systems. Their low output power, once a limitation, now matches embedded systems' energy budgets. Amato et al. first demonstrated a tunnel diode as a reflection amplifier for backscatter, achieving kilometer-range links at microwatt power [2], though the architecture retained dependence on an ED. To eliminate ED dependence, subsequent work revived the TDO, a topology dating to the early 1960s [109], and applied it to transmitter design [103].

The standard TDO topology couples a tunnel diode to an LC tank, generating a carrier at microwatt power [65, 96, 103]. LC-tank-based TDOs exhibit frequency instability, drifting hundreds of kHz to MHz under environmental changes, with high phase noise restricting modulation to simple on-off keying (OOK) at low bitrates [103]. Later systems addressed this through injection locking from an external ED [58, 104], relaxing its power requirement but preserving the three-device topology. More recent work pursues standalone operation through voltage-transition [65], voltage-conditioning techniques, electromagnetic shielding, and supply noise reduction [77]. None address the fundamental limitation. *An LC tank provides insufficient Q-factor for a stable TDO*, resulting in MHz-scale drifts under supply voltage and temperature variations. No prior system has demonstrated a frequency-stable TDO suitable for microwave transmitter and receiver design without an ED.

The Q-factor determines the sharpness of an oscillator's frequency response. A low-Q resonator produces a broad spectral peak, high phase noise, and is sensitive to supply voltage [65, 99], temperature [65, 99], and nearby motion [96], degrading link reliability as the carrier drifts outside the receiver's passband. Classical TDOs [13, 31, 58, 60, 65, 66, 77, 96, 99, 103, 104] rely on LC tanks built from discrete inductors and capacitors storing energy in electromagnetic fields around component leads and pads. At UHF frequencies, parasitic winding resistance, skin-effect losses, and substrate dielectric losses dissipate an increasing stored energy each cycle. These parasitics are environmentally coupled. Nearby conductors alter stray capacitance, vibration shifts geometry, and temperature modifies inductance and capacitance. The oscillator's frequency is thus set not by a precisely defined structure but by lossy, environmentally sensitive lumped elements, limiting Q to typically below 100. This produces poor stability in classical LC-tank based TDO designs and necessitates an ED for injection locking in transmitter [104] and receiver [58] designs.

A surface acoustic wave (SAW) resonator confines energy in a mechanical standing wave on a piezoelectric substrate, where the resonant frequency is set lithographically by electrode pitch rather than discrete component values [72, 115]. The acoustic wavelength at UHF is in micrometer-scale, concentrating energy with minimal radiative loss, yielding Q-factors exceeding 1000, an order of magnitude above lumped LC tanks. This distinction (mechanical acoustic cavity versus electromagnetic fields around discrete components) and the resulting high Q-factor motivate coupling a tunnel diode to a SAW resonator. We show that this yields a highly stable TDO, which we call the Resonator Tunnel Oscillator (RTO).

However, realizing this combination presents a non-trivial design challenge. A SAW resonator is a narrow-bandwidth impedance element, fundamentally different from the broadband LC tank that TDO circuits traditionally assume. This mismatch likely explains why, despite their half-century history, they were never combined to produce a stable oscillator. M^2 introduces a biasing and matching topology that sustains stable oscillation by operating the tunnel diode within its NDR region while satisfying the SAW resonator's impedance constraints at 433 MHz. The resulting oscillator is a two-terminal device requiring only a DC supply, no external carrier signal or ED, no injection locking, and no phase-locked loop.

Through controlled experiments, we find that M^2 consumes 105 µW peak power, of which only 35 µW is attributable to the SAW resonator. In free-running mode, the maximum frequency drift is hundreds of Hz over 4 hours and just under 1 kHz over 14 hours as observed in Figure 1(a). This stability holds when substituting tunnel diodes of the same type or replacing them with a different type entirely, confirming that frequency stability is conferred by the SAW resonator, not any individual diode. Under controlled temperature and humidity variation, often exceeding real-world conditions, frequency deviation remains within 46 kHz, at least two orders of magnitude better than state-of-the-art LC-based TDOs [77]. In uncontrolled environments, including a busy university food court and direct sun with high humidity, deviation stays at tens of kHz, still orders of magnitude below LC-based TDOs in benign conditions.

We use M² as a building block to realize both a transmitter and a receiver, as shown in Figure 2, demonstrating that a single microwatt-class component can serve both roles in a link. Beyond carrier signal generation, each role requires frequency conversion. A transmitter must upconvert a baseband signal onto the carrier, while a receiver must downconvert an incoming RF signal to an intermediate frequency (IF) for demodulation. Both operations require a mixer, another power-consuming analog component. M² addresses this by exploiting two properties of TDO. Self-oscillating mixing (SoM) lets the oscillator simultaneously generate a carrier and modulate it with an input signal [104], while autodyning [58] uses the TDO as its own local oscillator to downconvert received signals. Both have been demonstrated in LC-based TDOs [58, 104]; our experiments confirm they are preserved with a SAW resonator, enabling the standalone transmitter and receiver in Figure 2.

While SoM in M² exhibits higher conversion loss and nonlinear behavior than LC-based TDOs due to the SAW resonator's narrowband impedance, the resulting transmitter achieves 135 m line-of-sight range, 46 m in complex non-line-of-sight environments, and bitrates up to 100 kbps using 2-FSK modulation. The autodyning receiver, conversely, benefits from the SAW resonator. Downconversion loss at lower IF frequencies is at least 10 dB below LC-based TDO receivers, and reception sensitivity reaches −75 dBm, surpassing prior TDO-based receivers [58]. The receiver's higher sensitivity, combined with the transmitter's longer ED-free range, enables symmetric M² links and a step towards tag-to-tag networks [50].

Summary of Results. We offer the following key results:

- M² generates a carrier with spectral purity and phase-noise performance comparable to an SDR, consuming only 105 μW while maintaining stability below 2.10 ppm over a four-hour period.
- M² enables tag-to-tag communication at up to 40 m indoors without any external carrier source or active transceiver.

2 Background

Low-power networks. Two decades of work on sensor networks have targeted applications such as habitat monitoring [51], volcano monitoring [110], and infrastructure such as bridges [9], and explored mesh networking and its multihop tradeoffs including routing decisions and link reliability. All were fundamentally constrained by the milliwatt power consumption of their transceivers. By enabling microwatt-power transmission and reception, M² can substantially extend the operational lifetime of sensor networks.

Backscatter systems. The most widespread backscatter system is RFID [106, 108], in which a reader serves as both an ED and a receiver. This is a monostatic configuration and suffers from self-interference [100]. Modern systems address this by separating the ED and receiver in a bistatic configuration, reducing self-interference via path loss and enabling commodity devices such as Wi-Fi routers [71, 100] and smartphones [38] to serve as EDs. This architecture has yielded transmitters compatible with Wi-Fi [38, 42, 124], Bluetooth [20, 38, 118], ZigBee [38, 124], and LoRa [70, 91, 124], with subsequent efforts extending ranges to kilometers by trading bitrate [70, 91, 100] for sensitivity and exploring large-scale deployments [5, 33, 101]. These systems, however, depend on EDs that must typically transmit at maximum legal power [42, 91]. M² eliminates the need for EDs by enabling standalone transceivers.

Reflection amplifiers. These mitigate the need for a proximate ED by compensating for the backscatter tag's reflection loss. Transistor-based designs consume hundreds of microwatts [46], while tunnel-diode based designs operates at tens of microwatts [2, 17, 103]. Although the ED can operate farther from the tag, the system still requires one, and reflection amplifiers inherently generate strong harmonics due to their nonlinear nature, impairing link reliability and network coexistence. M² takes a major step towards eliminating the ED by enabling design of standalone transmitters.

Schottky-diode receivers. Schottky-diode receivers support low-power reception by extracting the envelope directly or mixing with an external signal for IF downconversion. Envelope detectors extract the power envelope of incoming signals and are integral to RFID [29, 64], but lack frequency selectivity, cannot demodulate phase or frequency information, and are limited to OOK. Amplifiers and SAW filters extend their capabilities [14, 32], yet they still cannot recover an IF signal for complete demodulation. More recent designs exploit Schottky-diode nonlinearity to mix incoming signals with an external carrier for IF downconversion, enabling low-power BLE [19] and ZigBee receivers [74], though sensitivity remains limited by the Schottky diode. EDISON [25] used Li-Fi instead of RF for the downlink to overcome envelope-detector constraints. Envelope detectors have also found application in accurate localization [26] and low-power audio reception [92]. M² enables ED-free reception with IF downconversion and high sensitivity. In tag-to-tag networks, M² achieves tens of meters with IF downconversion, whereas state-of-the-art envelope detectors extract only amplitude at ranges of a few meters and low bitrates. A detailed comparison of receivers is provided in Table 2.

Tag-to-tag networks. Ambient backscatter [50] demonstrated that backscattering ambient TV signals enables battery-free communication while harvesting energy from the environment. Parks et al. extended range to a few meters by trading bitrate for coding gain [69], Majid et al. demonstrated multihop networking using a powerful RFID reader as ED [52], and Ryoo et al. applied tag-to-tag networks to activity recognition [79]. These systems are constrained by the short range of Schottky diode envelope detectors and require a carrier from a dedicated ED or ambient source. M² eliminates the need for both an ambient carrier and an ED. Moreover, through improved receiver sensitivity via autodyning, M² supports ranges of tens of meters for practical tag-to-tag networks.

Tunnel-diode transmitters. These couple a tunnel diode with an LC tank, whose low Q produces frequency instability far short of commodity standards [66, 76, 77], with drifts of several MHz under voltage and environmental fluctuations that severely limit link reliability. As an example, SharpPeak attempts to stabilize classical LC-tank-based TDOs but reports frequency drifts in MHz under bias voltage and temperature changes [65, 66], while using these voltage changes for modulation. SharpPeak couples the carrier frequency to the modulating signal, resulting in unstable communication and making coexistence challenging. M² instead performs modulation through SoM, where the SAW-anchored carrier remains fixed and only the sidebands carry the baseband signal, preserving

System / Work	Frequency band (MHz)	Bitrate (bps)	External carrier[1] (dBm)	Power consumption (μW)	Range (m)
HitchHike (2016) [119]	2400	222k	30 (1 m)	33	54
LoRea (2017) [100]	868	2.9k	28 (1 m)	70	3400
LoRea (2017) [100]	2400	2.9k	26 (1 m)	650	255
LoRa BS (2017) [91]	915	50	30 (5 m)	9.25[2]	2800
5.8 GHz[4] (2018) [17]	5800	N/R	N/R	20	48 dB[5]
P2LoRa (2021) [39]	433	111	30 (1 m)	320	2200
Judo (2022) [104]	868	100k	25 (> 100 m)	< 100[3]	100
SlimWiFi (2023) [122]	2400	100k	—	1000	60
FM Rider (2024) [114]	88-108	200	-40 (Ambient)	1440	107
AudioCast (2025) [77]	88-108	10.7k	—	200	130
This work	**433**	**100k**	**Not required**	< 105	**135 m**

N/R: Not reported [1] Marked with the transmission strength of ED wherever used. The distance in braces is the ED-to-tag distance. [2] IC simulation power [3] Frontend and baseband generator power [4] Reflection amplifiers [5] Reflection amplifier tag reports 48 dB gain; distance not explicitly reported

Table 1: Low-power transmitter comparison. Columns report band, bitrate, whether an ED is required (and its strength), transmitter power, and range.

carrier stability during transmission. M^2 overcomes these limitations by integrating a tunnel diode with a high-Q SAW resonator, achieving at least an order of magnitude higher frequency stability and substantially greater robustness to bias voltage fluctuations and temperature changes, while generating a stable carrier at lower power, even compared to conventional oscillators consuming orders of magnitude more. M^2 further demonstrates autodyning, enabling a complete transceiver design. This stability holds in complex environments such as a busy food court and outdoors, with drift of only a few kHz, enabling a new class of tag-to-tag networks, as demonstrated in Section 4.2. Table 1 compares transmitter designs including tunnel-diode transmitters. Figure 27 and Appendix E compare prior architectures.

SoTA oscillators. Low-power oscillators span ring, LC/DCO, and resonator-referenced designs compared in Table 5 and Appendix A. Each family makes distinct tradeoffs. Ring oscillators without a crystal reference cannot guarantee ppm stability and require receiver assistance or injection locking [53, 111]. LC oscillators improve phase noise but at the cost of higher current and larger area; commercial VCOs draw several milliwatts, often unacceptable for battery-free devices [55–57]. SAW-resonator oscillators offer tight tolerance and low temperature coefficients, but are fixed-frequency with limited pulling range and modest output [28, 62, 113, 121]. All families remain susceptible to temperature drift, aging, and supply-voltage variations. M^2 bridges this gap by coupling a tunnel diode with a high-Q SAW resonator, yielding a microwatt-scale oscillator with practical stability that enables standalone transceiver design.

SAW resonators. Surface acoustic waves were first described by Rayleigh [75]. Modern SAW resonators owe their design to the interdigital transducer (IDT), demonstrated by White and Voltmer in 1965 [112], in which interleaved electrodes on a piezoelectric substrate launch and receive surface acoustic waves. Their superior Q-factor enabled widespread use in the 1970s-80s at hundreds of MHz for military radar [67], and as oscillator elements in radio and television tuners [16, 83, 115]. In the early 1990s, SAW ladder filters entered cellular handset front-ends [37], and temperature-compensated variants [80] further improved stability for tighter channel spacing. More recently, SAW resonators have coupled microwave signals to photons in integrated photonic circuits [82] and enabled on-chip acousto-optic modulation [47]. The practical SAW resonator emerged in the early 1970s, more than a decade after Esaki discovered the tunnel diode in 1957 [21, 24]. Yet as SAW technology matured, tunnel diodes fell out of favor, replaced by three-terminal transistors offering input-output isolation and easier integration. Their low output power was seen as a limitation rather than an advantage, and the two never converged until M^2.

System / Work	Frequency band (MHz)	Bitrate (bps)	External carrier[1]	Power consumption (μW)	Sensitivity (dBm)
2.4 GHz Rx (2017) [19]	2400	1M	Required	N/R[2]	N/R
802.15.4 Rx (2018) [74]	2400	250k	Required	361	−48
MIXIQ (2021) [78]	2400	1125k	Helper tone	300	−55
Passive DSSS (2022) [48]	915/2400[3]	1k	—	166.5	−46
OFDMA Rx (2022) [123]	2400	N/R	—	652[4]	−27[5]
Saiyan (2022) [30, 32]	433	1k	—	369.4	−43
μmote (2023) [86]	915	2k	Required	62.07	−48
Sisyphus (2024) [105]	433	up to 19k	—	162.7	−42
SoMix (2025) [58]	868	up to 10k	Optional	100	−70
This work	**433**	~ 10k	**Not required**	<105	-75

N/R: Not reported [1] Marked wherever an external signal assists the RX front-end [2] Proof-of-concept; passive diode mixer [3] DSSS receiver; prototyped for 915/2400 MHz; [4] With 1% duty-cycling [5] When receiving one sub-carrier

Table 2: Low-power receiver comparison. Columns report band, bitrate, front-end power, and sensitivity where available. For ED-assisted systems, sensitivity depends on ED-to-tag distance and the carrier signal strength.

3 Design

The microwave oscillator is the most power-consuming component of a radio transceiver [19, 20, 42, 50, 69, 100]. In transmission, the oscillator generates the carrier signal, which is modulated with a baseband signal and amplified. In reception, an LNA amplifies incoming signals, which are mixed with a local carrier signal for downconversion to an IF signal. These analog tasks (carrier generation, mixing, and amplification) dominate the power budget. M^2 uses a tunnel diode to consolidate these steps into a single circuit, eliminating discrete mixers, oscillators, and amplifiers. This unified architecture reduces power consumption of the M^2 frontend to under 70 µW, and 105 µW with the SAW resonator included.

Oscillator design. An oscillator sustains energy oscillation within a resonant structure. At microwave frequencies, resistive losses, radiation, and parasitic coupling dissipate stored energy each cycle. A negative-resistance device such as a tunnel diode, biased within its NDR region, replenishes this energy by presenting negative conductance to the circuit. When this negative conductance equals or exceeds the total loss conductance, oscillation becomes self-sustaining; steady-state amplitude is reached when large-signal average negative conductance exactly balances losses. The resonant structure determines frequency, but its quality factor Q (the ratio of stored to dissipated energy per cycle) governs stability, phase noise, and consequently link quality in communication.

Tunnel diodes. They are devices with heavily doped p-n junctions that enable band-to-band tunneling [27, 61, 81]. They were discovered in the 1950s [21], and were the first semiconductor device to demonstrate quantum tunneling. They are typically fabricated from germanium or gallium arsenide. When biased near zero volts, electrons tunnel through the narrow depletion region rather than surmounting the energy barrier, producing a sharp current increase followed by a decrease as bias voltage rises. The resulting nonlinear I-V curves in Figure 3, were characterized using a Keysight *B2902A* Precision Source/Measure Unit [43]. Fast tunneling dynamics support operation up to low-GHz frequencies, and the low bias voltage and current at which NDR occurs enables microwatt operation.

Tunnel diode oscillators. From the earliest days following Esaki's discovery [21], researchers explored the potential of TDOs. Sommers demonstrated an LC-tank TDO at 1.4 GHz in 1959 [85]. Kim

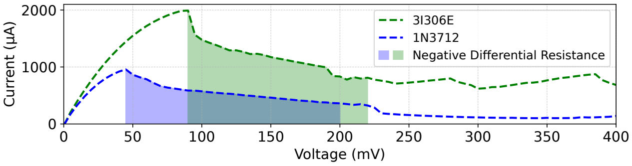

Figure 3: I-V characteristics of two tunnel diodes used in this work, the GE 1N3712 and the GaAs 3I306E. The shaded region indicates the NDR region.

and Brandli presented an LC-tank TDO reaching 2 GHz to 3 GHz at 1 mW output [44], while Hines provided a theoretical framework [34]. These designs consumed milliwatts and offered poor stability, as the broadband LC tank provided no mechanism to constrain oscillation. Van Degrift achieved remarkable 0.001 ppm precision at microwatt power [98], but only at cryogenic temperatures below 10 K and frequencies below 10 MHz. Young, Burrus, and Shaw demonstrated a 50 GHz TDO embedded in a rectangular waveguide, at milliwatt-level power [116]. Sterzer and Nelson demonstrated TDO from 610 MHz to 8.35 GHz at milliwatt power [87]. Clover and Wolf demonstrated a TDO at 3 MHz to 55 MHz for magnetic susceptibility measurements, operating from 1.2 K to 300 K in fields up to 1.8 T [11], achieving approximately 1 ppm stability at room temperature but with significant frequency dependence on bias voltage and mechanical perturbations. Watters departed from LC-tank based designs by coupling a tunnel diode with an 18 MHz bulk quartz crystal [109]. As transistor technology matured, interest in tunnel diodes for mainstream RF applications declined, though they persisted in specialized roles such as satellite receivers [35].

M² builds on recent efforts reviving the tunnel diode for low-power communication. Amato et al. showed a reflection amplifier [2, 3], and Eid et al. presented both a reflection amplifier and oscillator [17]. TunnelScatter presented a TDO with LC tank and reflection amplifier at 868 MHz [103], but highlighted inherent instability, limiting modulation to OOK. TunnelEmitter designed a battery-free carrier emitter but suffered from severe frequency instability [99]. TunnelSense exploited this instability as a feature, using drift to sense gestures and breathing [96]. Other efforts tackled stability through injection locking with an external signal [58, 60, 104], while the most relevant prior work addressed TDO instability through RF shielding, careful bias control, frequency selection, and noise reduction [65, 77]. All remain limited by the low Q of the LC tank, which is not an engineering shortcoming but a consequence of electromagnetic energy storage in discrete components. M² addresses this root cause by replacing the LC tank with a SAW resonator, generating a stable carrier signal at 433 MHz.

3.1 Resonator Tunnel Oscillator

We describe the RTO, which is the core of M².

SAW resonators overview. A SAW resonator consists of an IDT that excites surface acoustic waves on a piezoelectric substrate. Distributed Bragg reflectors on either side of the IDT reflect acoustic energy back toward the transducer, forming a standing wave within a resonant cavity. The resonant frequency is determined by the IDT electrode pitch, $f_0 = v_s/\lambda$, where v_s is the surface acoustic wave velocity in the substrate (typically 3,000–4,000 m/s for quartz and lithium tantalate) and λ is set lithographically by electrode periodicity. Unlike an LC tank, whose frequency depends on discrete component values, f_0 in a SAW resonator is fixed at fabrication and insensitive to the electrical bias conditions of any connected circuit, leading to the improved stability we observe in M².

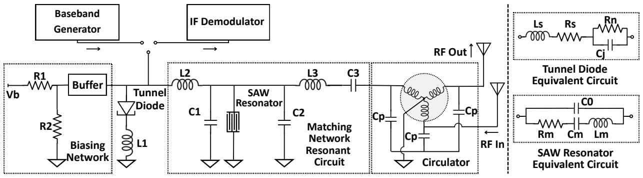

Figure 4: The SAW resonator fixes the oscillation frequency while the tunnel diode provides negative resistance to sustain oscillation, generating a stable carrier. Self-oscillating mixing and autodyning properties enable transmission and reception respectively, without additional mixer stages.

3.1.1 *Resonator Tunnel Oscillator Challenges and Design.*

We discuss the challenges of coupling a tunnel diode to a SAW resonator and describe how the RTO addresses them.

Equivalent circuit. The electrical behavior of a one-port SAW resonator near resonance is captured by the Butterworth-Van Dyke circuit shown in Figure 4, comprising a series branch of motional inductance L_m, capacitance C_m, and resistance R_m in parallel with static electrode capacitance C_0. The motional arm represents the mechanical resonance, with L_m and C_m setting the series resonant frequency $f_s = 1/(2\pi\sqrt{L_m C_m})$ and R_m capturing acoustic losses to determine $Q = 2\pi f_s L_m/R_m$. The parallel resonant frequency f_p, where impedance reaches its maximum, occurs slightly above f_s at a separation governed by the capacitance ratio $r = C_0/C_m$. Between f_s and f_p, the resonator presents an inductive impedance; outside this band, it is capacitive. For the 433 MHz SAW resonator in M², this inductive window spans only a few hundred kHz, three orders of magnitude narrower than a lumped LC tank at the same frequency.

Oscillator design challenges. The narrow inductive bandwidth of the SAW resonator has a direct consequence for oscillator design. A negative-resistance oscillator requires two conditions simultaneously at the desired frequency ω_0. First, the total circuit reactance must vanish, $X_{\text{tot}}(\omega_0) = 0$. Second, the tunnel diode's negative conductance must exceed the total loss conductance of the network. In a classical LC-tank TDO, the inductor presents smoothly varying reactance over tens of MHz, satisfying these conditions loosely across a broad range. Oscillation starts easily but settles at whatever frequency the reactance happens to cancel, drifting with temperature, supply voltage, and parasitic coupling. A SAW resonator fundamentally changes this. It presents inductive reactance only within the narrow window between f_s and f_p; outside this window, it is capacitive and cannot sustain oscillation.

The narrow inductive window that gives SAW resonators their stability also makes design harder. If the tunnel diode and surrounding network do not satisfy both oscillation conditions simultaneously at the SAW resonant frequency, the circuit either fails to oscillate or locks to a spurious LC-dominated mode with poor stability. The challenge is compounded by the tunnel diode's nonlinear, bias-dependent impedance, whose effective negative conductance shifts with operating point and determines whether the oscillation conditions are met within or outside the SAW resonator's inductive window. Satisfying both conditions within a span of only a few hundred kHz, while accommodating this nonlinearity and preserving the SoM and autodyning capability needed for transmission and reception, is the core challenge that M² tackles.

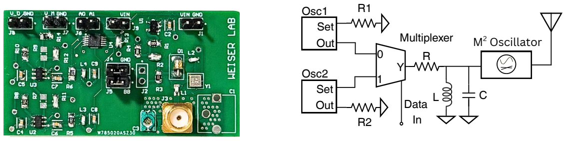

(a) Transmitter Prototype (b) Transmitter Circuit

Figure 5: Schematic and hardware prototype of a 2-FSK M² transmitter instantiated using the RTO, which does not require an emitter device.

RTO design philosophy. M² decouples frequency stability from the tunnel diode by assigning each component a distinct role. The SAW resonator acts as an acoustic flywheel. Once energy is stored in its mechanical standing wave, the crystalline substrate sustains oscillation at its lithographically defined frequency with minimal loss, resisting perturbations just as a massive flywheel resists changes to its rotational velocity. The tunnel diode serves solely as a low-power negative-resistance element that replenishes the energy dissipated each cycle, without determining the oscillation frequency. Perturbations that would shift a classical TDO by tens of kHz, such as supply voltage fluctuations, thermal drift, or nearby motion, now encounter the full inertia of the SAW resonator's high-Q mechanical resonance. In essence, the tunnel diode decides *whether* the circuit oscillates; the SAW resonator decides *where*.

RTO matching and biasing network. As shown in Figure 4, M² employs a matching network (C_1, C_2, L_2, L_3) between the tunnel diode and SAW resonator port that transforms the diode's impedance to match the resonator's motional impedance at f_0, cancels the total circuit reactance within the inductive window, and provides sufficient negative conductance margin to overcome R_m. A variable capacitor enables fine alignment of the reactance cancellation point to the SAW resonator's narrow bandwidth; without this tunability, fabrication tolerances would place the reactance zero outside the inductive window, preventing oscillation. The bias network is equally critical. The tunnel diode must operate at a precise point within its NDR region, since a bias too close to the peak provides insufficient negative conductance to sustain oscillation, while too close to the valley reduces voltage swing and output power. M² generates the bias through a resistive divider with impedance significantly higher than the resonator's at f_0, avoiding RF loading, and uses a continuous ground plane beneath the RF path to suppress parasitic coupling between DC and RF domains.

Preserving nonlinearity in RTO. Beyond stable oscillation, the matching network must preserve the tunnel diode's nonlinear I-V characteristic, which enables M² to function as both transmitter and receiver. In transmission, this nonlinearity performs SoM, generating products at $f_0 \pm f_{\text{baseband}}$ that upconvert the signal without a separate mixer. In reception, the same nonlinearity enables autodyning, where an incoming RF signal near f_0 interacts with the self-generated carrier to produce an IF signal. Over-constraining the diode's impedance to maximize stability attenuates these mixing products. M² balances this tradeoff by presenting high impedance at f_0 to anchor the carrier while allowing the diode to respond at the offset frequencies $f_0 \pm f_{\text{IF}}$. The baseband signal is injected through a high-value resistance that permits modulation to reach the diode's bias point without disturbing the RF impedance at the tunnel diode, decoupling the modulation path from the resonant circuit.

RTO implementation. We implemented M² on a PCB fabricated on an FR-4 substrate, as shown in Figure 1(b). RTO pairs a GE 1N3712 tunnel diode [18] with a 433 MHz SAW resonator [90]. A voltage regulator (S-1313) [1] and resistive divider network maintain the diode in its NDR region, and an LC network compensates for the parasitic lead inductance and junction capacitance of the tunnel diode. The RF output is routed to an SMA connector, enabling characterization via coaxial cable or transmission and reception through an antenna. The complete circuit schematic appears in Figure 4, and the M² transmitter prototype in Figure 5.

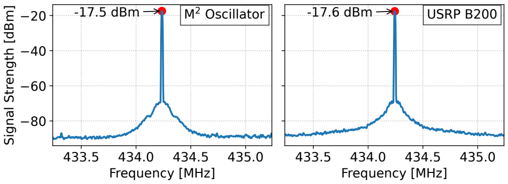

Figure 6: The carrier signal generated by the RTO exhibits high spectral purity, comparable to a commercial USRP SDR at the same output power.

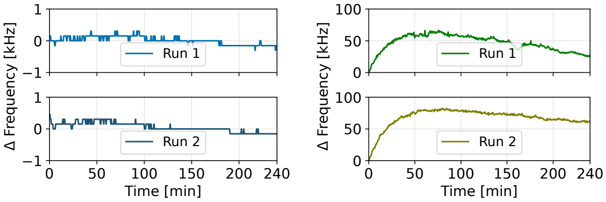

(a) Resonator Tunnel Oscillator (b) Classical Tunnel Diode Oscillator

Figure 7: The RTO maintains two orders of magnitude better stability than a classical TDO. Over 4 hours**, the absolute RTO drift stays below** 316 Hz**, whereas the classical TDO drifts tens of** kHz **from the resonant frequency.**

RTO power-consumption. We measure the power consumption of M² using a precision voltage source. The 1N3712 tunnel diode is biased at 156 mV, and the complete frontend including the SAW resonator consumes less than 105 µW. Without the SAW resonator, consumption is 70 µW, indicating that the resonator adds only 35 µW. Practical deployments require a stable bias network to maintain the diode's operating point; we implement this using a resistive divider (Figure 4) consuming a few hundred microwatts, which can be further reduced through high-value resistors. Notably, M² does not require active temperature compensation. As we demonstrate in Section 3.1.2, ambient temperature variations in real-world deployments do not significantly impact frequency stability.

Putting everything together. The oscillator generates a carrier at 434 MHz with a measured signal strength of −17.5 dBm, as shown in Figure 6. The carrier exhibits high spectral purity, and a comparison with a signal generated by a USRP software-defined radio at the same power level shows the two are visually indistinguishable, demonstrating that M² achieves carrier quality comparable to conventional oscillators that consume orders of magnitude more power. Combined with the SoM and autodyning properties preserved by the matching network, this oscillator serves as the building block for both a standalone transmitter and receiver.

3.1.2 *Understanding and Characterizing Stability.*

We characterize the stability that the SAW resonator confers on the tunnel diode oscillator through systematic experiments.

Quality factor and frequency stability. The oscillation frequency ω_0 of the RTO is set by the reactive condition using the reactive Barkhausen condition for oscillation as $X_{\text{tot}}(\omega_0) = 0$, where

$$X_{\text{tot}}(\omega) = X_{\text{TD}}(\omega) + X_{\text{tank}}(\omega) \tag{1}$$

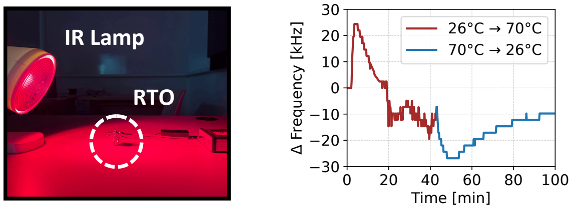

(a) Evaluation Setup (b) Effect with Temperature

Figure 8: Under temperature changes exceeding typical deployment conditions, the RTO's frequency drift remains within 45 kHz**. A slight hysteresis between heating and cooling traces is attributable to thermal expansion of PCB traces.**

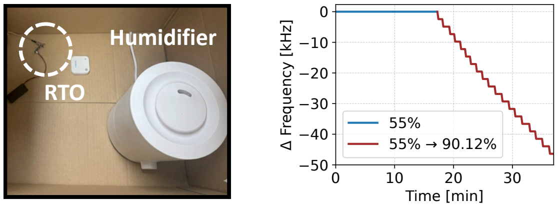

(a) Evaluation Setup (b) Effect with Humidity

Figure 9: The RTO exhibits small frequency shifts with increasing humidity, staying within 46 kHz **even at high humidity.**

is the reactance of the tunnel diode and the LC–SAW resonant network including antenna loading of the circuit as in the Figure 4. A convenient way to quantify the frequency stability of the oscillator is via the *reactance slope parameter* at the oscillation frequency,

$$S_X \equiv \left.\frac{dX_{\text{tot}}}{d\omega}\right|_{\omega_0} \tag{2}$$

Consider a small perturbation ΔX due to bias-dependent parasitics or changes in antenna environment that appears as additional reactance. The new oscillation frequency $\omega_0 + \Delta\omega$ still satisfies,

$$X_{\text{tot}}(\omega_0 + \Delta\omega) + \Delta X \approx 0 \tag{3}$$

Using a Taylor series expansion of $X_{\text{tot}}(\omega_0 + \Delta\omega)$ around ω_0 and retaining only the first-order term, we obtain $X_{\text{tot}}(\omega_0 + \Delta\omega) \approx X_{\text{tot}}(\omega_0) + (dX_{\text{tot}}/d\omega)|_{\omega_0}\,\Delta\omega$. Substituting this into the Equation 3, using $X_{\text{tot}}(\omega_0) \approx 0$, and Equation 2 we get,

$$\Delta\omega \approx -\frac{\Delta X}{\left.\frac{dX_{\text{tot}}}{d\omega}\right|_{\omega_0}} \approx -\frac{\Delta X}{S_X} \tag{4}$$

Hence a large reactance slope S_X makes the oscillation frequency stiff with respect to small reactive perturbations, while a small S_X leads to strong frequency pulling due to any parasitic changes. For a standard series RLC resonant circuit with impedance $Z(\omega) = R + j(\omega L - (\omega C)^{-1})$, the reactance is $X(\omega) = \omega L - 1/(\omega C)$. Differentiating with respect to ω and evaluating at the resonant frequency $\omega_0 = 1/\sqrt{LC}$, where $1/(\omega_0 C) = \omega_0 L$, we obtain,

$$\left.\frac{dX}{d\omega}\right|_{\omega_0} = L + \frac{1}{\omega_0^2 C} = 2L. \tag{5}$$

The Q-factor can then be written as

$$Q = \frac{\omega_0 L}{R} = \frac{\omega_0}{2R}\left.\frac{dX}{d\omega}\right|_{\omega_0} = \frac{\omega_0}{2R}S_X \tag{6}$$

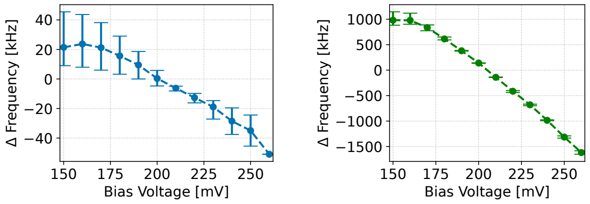

(a) Resonator Tunnel Oscillator (b) Classical Tunnel Diode Oscillator

Figure 10: A classical TDO behaves as a VCO, drifting several MHz **under bias voltage changes. The RTO drifts under** 70 kHz **in identical conditions, as bias-induced shifts in the diode's junction capacitance slightly perturb the matching network rather than directly changing the oscillation frequency.**

This relation generalises to any one-port series resonator. The product $\omega_0 S_X/(2R_{\text{eq}})$ is the loaded quality factor Q_{L}, where R_{eq} is the equivalent series resistance at resonance. Combining the Equations 4 and 6 gives a simple approximation for frequency pulling due to a small perturbing reactance ΔX as given below,

$$\frac{\Delta\omega}{\omega_0} \approx -\frac{\Delta X}{\omega_0 S_X} = -\frac{\Delta X}{2R_{\text{eq}}Q_{\text{L}}} \tag{7}$$

We therefore interpret $K \equiv \omega_0 S_X = 2R_{\text{eq}}Q_{\text{L}}$ as a reactance-slope based stability factor. A higher K, or equivalently, a higher loaded Q—factor directly attenuates the relative frequency shift for a given perturbation ΔX. In the M², S_X is dominated by the steep reactance slope of the SAW resonator, effectively pinning the oscillation to the acoustic resonance. Compared to a conventional LC-based TDO, this results in a significantly larger K, thereby minimizing frequency instability from external factors.

Baseline stability. We evaluate the RTO's stability by connecting it directly to a spectrum analyzer (SignalHound BB60C [36]) via coaxial cable, minimizing external interference to establish baseline stability. The setup is placed in an isolated, air-conditioned room with restricted access. We continuously monitor signal strength and frequency across multiple four-hour runs. Figure 7 shows the results. The absolute RTO drift stays below 316 Hz, compared to over 50 kHz for classical TDOs. The RTO thus maintains stability two orders of magnitude better than classical TDOs [99, 103].

Extended stability. We conduct an experiment to investigate long-term stability, extending the measurement to 14 hours in the same controlled environment with an identical setup. Figure 1(a) shows a maximum absolute frequency drift of 916 Hz. The trace exhibits small abrupt frequency shifts, attributable to air-conditioning cycling that produces thermal fluctuations slightly altering the acoustic velocity of the SAW resonator. Even so, the total frequency drift remains below 1 kHz, comparable to state-of-the-art low-power oscillators shown in Table 5 and significantly better than existing TDO designs [31, 65, 76, 77, 99, 103].

Temperature stability. We evaluate the RTO under controlled temperature changes by heating the board with an infrared lamp and monitoring temperature with a non-contact thermometer, with the RTO connected to a spectrum analyzer via coaxial cable (Figure 8(a)). As shown in Figure 8(b), increasing temperature from 26 °C to 70 °C produces a maximum shift of 45 kHz, consistent with the parabolic temperature characteristic of SAW resonators [68, 80] and the thermal response of PCB traces and surrounding passives. We also observe hysteresis during cooling, where the frequency does not fully retrace the heating trajectory, as thermal gradients between the resonator and its mounting structure require time to equilibrate [68, 80]. Despite a 44 °C swing well beyond typical

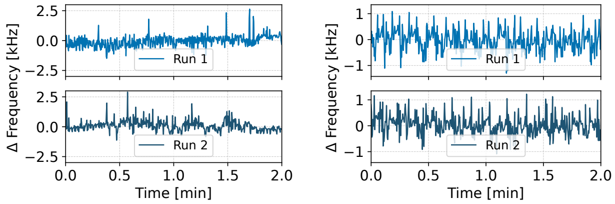

(a) Hand Gestures near RTO (b) Walking near RTO

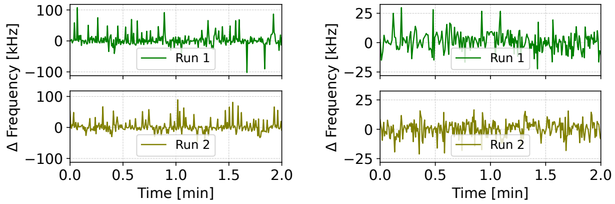

(c) Hand Gestures near TDO (d) Walking near TDO

Figure 11: Nearby motion causes only a few kHz of deviation in the RTO, whereas a classical TDO drifts by tens to hundreds of kHz under identical conditions. This suggests that the SAW resonator's mechanical resonance, and hence the RTO, is largely immune to ambient perturbations.

operating conditions, total drift remains within 45 kHz, at least two orders of magnitude smaller than TDOs under comparable conditions, consistent with existing efforts [65, 99].

Humidity stability. We evaluate humidity sensitivity by placing a humidifier near the RTO board and monitoring humidity with a co-located sensor, as shown in Figure 9(a). Figure 9(b) shows that increasing humidity from 55 % to 90 % decreases RTO frequency linearly by 46 kHz. This is consistent with moisture adsorption on the substrate surface, which increases effective mass loading on the SAW resonator and reduces acoustic wave velocity [72]. Despite this sensitivity, the RTO drift remains small, and the total frequency deviation under both temperature and humidity variation remains orders of magnitude below LC-based classical TDOs.

Bias voltage. A classical TDO behaves as a voltage-controlled oscillator (VCO), where even small bias voltage fluctuations induce significant frequency shifts in the resonant frequency of the TDO [65, 99]. We characterize RTO sensitivity to changes in the bias voltage using a direct coaxial connection to the spectrum analyzer, sweeping bias voltage from 150 mV to 260 mV in 10 mV steps via an Analog Discovery 3 voltage supply [12]. We compare this against a classical TDO evaluated as a baseline in the same experiment. As shown in Figure 10, the classical TDO exhibits the expected VCO behavior, drifting approximately 2.6 MHz across the voltage range. The RTO suppresses this effect, limiting total drift to under 70 kHz under identical conditions. The residual deviation is attributable to bias-dependent changes in the tunnel diode's junction capacitance slightly perturbing the matching network, rather than the VCO-like frequency pulling characteristic of classical TDOs [65, 99].

Nearby motion. Classical TDOs are highly susceptible to ambient perturbations, as even nearby motion such as walking or hand gestures can shift the resonant frequency. Although useful for sensing [96], this sensitivity is undesirable for communication. We evaluate the effect of nearby motion by connecting an antenna to the RTO and tracking its frequency with a spectrum analyzer at 1 m, then performing hand gestures and walking near the oscillator. Figure 11 shows that the RTO remains highly stable, with frequency drifts of only 4.12 kHz for hand gestures and 2.38 kHz for walking, compared to 135 kHz to 200 kHz and 44.45 kHz respectively for a classical TDO. The RTO substantially improves motion robustness even without shielding. As shown in Figure 12, adding a metallic shield (as demonstrated by AudioCast [77]) further reduces frequency drift due to hand gestures to 2.75 kHz.

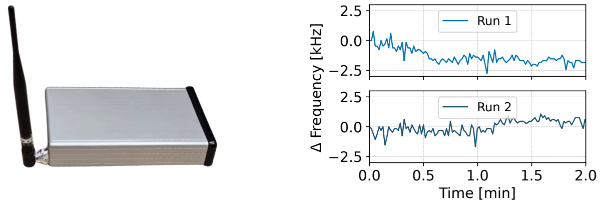

(a) Shielded Enclosure (b) Stability under Hand Gestures

Figure 12: A metallic enclosure further isolates the RTO circuit from environmental and near-field electromagnetic perturbations, thus reducing its frequency drift under nearby motion, including hand gestures, to 2.75 kHz.

Board	Tunnel Diode	Frequency Stability (ppm)	Amplitude Deviation (dB)
1	1N3712	2.10	0.309
2	1N3712	1.40	0.487
3	1N3712	1.40	0.708
4	3I306E	5.62	0.069

Table 3: Frequency stability and amplitude deviation across four M^2 boards over 4 hours of continuous operation. Boards 1–3 use the same tunnel diode type; Board 4 uses a different type, confirming that stability is conferred by the SAW resonator and not by the specific tunnel diode.

Tunnel diode variability. We assess the impact of tunnel diode variability on frequency stability and signal strength by swapping diodes of the same type and replacing the diode with an entirely different type. We prepare three RTO boards, each with a 1N3712 tunnel diode [18], and capture the generated signal using a spectrum analyzer in a cabled setup over four hours, tracking both frequency and amplitude. Table 3 presents the results. All three boards exhibit consistently high frequency stability, with only minor variation in signal amplitude attributable to differences in parasitic capacitance and lead inductance across individual diodes and boards.

To test generality, we replace the 1N3712 diode with a 3I306E tunnel diode [73], whose I-V characteristic is shown in Figure 3. Table 3 and Figure 26 show that the RTO with the 3I306E exhibits high stability; further details are provided in Appendix D. These results confirm that stability in M^2 is conferred by the SAW resonator rather than by the characteristics of any individual diode: the diode sustains oscillation, but the SAW dictates the frequency.

At microwave frequencies, external components such as cables, connectors, and probes introduce parasitics that perturb the SAW resonator's narrow resonance window, making initial oscillation lock sensitive to the parasitic environment. We address this by integrating the oscillator on a custom PCB with proper isolation, reducing uncontrolled parasitics, though small board-to-board frequency variations remain in our experiments. Future work could pursue SoC integration, following modern radio architectures.

Startup time. We measure startup time using a high-speed oscilloscope with one channel on the voltage supply and another on the RTO RF output, defining startup as the interval from power application to 90% of steady-state output amplitude. Across repeated measurements, RTO startup time is 359 ± 36 μs. This reflects the energy buildup dynamics of the high-Q SAW resonator, where the

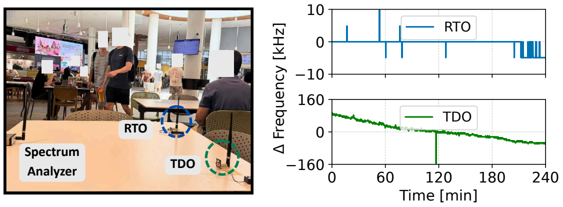

(a) Deployment in Food Court (b) Frequency Drift

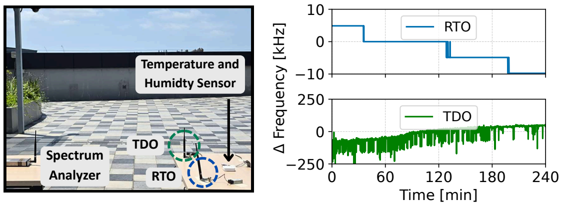

(c) Deployment on Rooftop (d) Frequency Drift

Figure 13: M² is deployed in two challenging real-world environments, a busy university food court during peak hours and a rooftop exposed to ambient weather changes. M² exhibits a maximum drift of only 15 kHz, whereas the classical TDO drifts by hundreds of kHz, confirming that the stability advantage persists well beyond controlled laboratory settings.

mechanical standing wave requires many acoustic cycles to reach steady state, and the cycle count scales proportionally with Q. The RTO is therefore inherently slower than a classical LC-tank TDO, whose low Q allows rapid buildup in microseconds, but significantly faster than crystal oscillators and phase-locked loops, which typically require milliseconds to achieve comparable stability.

Food court deployment. We evaluate the RTO in a busy university food court during lunch hours, with the spectrum analyzer placed 1 m from the oscillator. This is a challenging environment, where the RTO transmits wirelessly to the spectrum analyzer while exposed to continuous movement of students, staff, birds, and ambient airflow. Figures 13(a) and 13(b) show the setup and results. The RTO exhibits peak-to-peak frequency drift of only 15 kHz (34.56 ppm), whereas a classical LC-based TDO in the same setting drifts 250 kHz, more than an order of magnitude worse. This confirms that the SAW resonator's mechanical resonance is largely immune to the factors that destabilize LC tanks in crowded environments.

Rooftop deployment. We conduct a second uncontrolled experiment on a rooftop in the evening, as shown in Figure 13(c), with the RTO exposed to ambient temperature decreasing from 30 °C to 26 °C and relative humidity rising from 63% to 80% over the experiment duration. Even under these simultaneous, uncontrolled variations, the RTO exhibits only 15 kHz peak-to-peak drift, while the classical TDO drifts 310 kHz, as shown in Figure 13(d). In a separate experiment on a hot afternoon, with temperature varying from 35 °C to 46 °C and humidity from 35% to 50%, the RTO drift remains under 10 kHz. Across all deployments, the RTO maintains at least an order of magnitude better stability than the classical TDO, confirming that the stability observed in controlled experiments persists in real-world outdoor conditions.

3.1.3 *Characterizing Self-oscillating Mixing and Autodyning.*

Beyond oscillation, M² enables transceivers because the RTO exhibits SoM [104] and autodyning [58] properties. We conduct experiments to characterize the RTO's performance in these roles and quantify any trade-offs relative to the classical TDO.

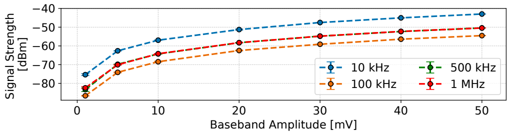

(a) Varying Baseband Amplitude

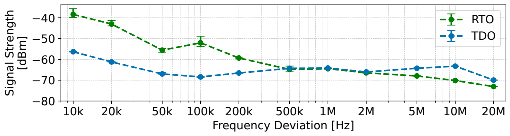

(b) Varying Baseband Frequency

Figure 14: The RTO preserves self-oscillating mixing with stable sidebands, though the SAW resonator's high Q introduces frequency-dependent attenuation of mixing products that increases with offset from the carrier.

Self-oscillating mixing. Tunnel diodes are highly nonlinear devices, and this nonlinearity enables mixing without a separate active mixer. Prior work has demonstrated SoM in TDOs, where the device simultaneously generates the carrier and mixes baseband signals for transmission [60, 104]. A key question for M² is whether coupling a high-Q SAW resonator to the tunnel diode preserves this property, since the resonator increases frequency selectivity.

To answer this, we compare the RTO against a classical TDO using controlled experiments. A waveform generator (Analog Discovery 3 [12]) provides baseband signals at swept amplitudes and frequencies, and a spectrum analyzer measures the resulting sidebands. Figure 14 confirms that SoM is preserved in the RTO, as the mixed sidebands appear clearly near the carrier and remain stable across the tested conditions. Both the TDO and RTO exhibit a frequency-dependent mixing response, with sideband strength decreasing at larger offsets from the carrier signal. In the RTO, this rolloff is steeper due to the SAW resonator's narrow bandwidth, which favors sidebands closer to the carrier. The practical consequence is not a loss of SoM capability but reduced sideband power at larger offsets, affecting modulation schemes requiring wider bandwidth. Within the SAW resonator's passband, however, the RTO achieves stable mixing with lower drift than the classical TDO.

Prior effort such as SharpPeak [65] exploits the VCO-like bias-to-frequency relationship of classical TDOs for modulation, but this couples carrier frequency directly to bias voltage, so supply noise and temperature drift translate into frequency instability. SoM in M² decouples these roles: the SAW-anchored carrier remains at f_0 while the baseband is upconverted to sidebands at $f_0 \pm f_{\text{baseband}}$, preserving ppm stability during modulation and enabling clean FDMA channel allocation as we show in Section 4.4.

Autodyning. Tunnel diode nonlinearity enables a second critical function, downconversion. SoMix [58] shows that a TDO can act as an autodyne mixer, simultaneously serving as the local oscillator and downconverting an RF signal to IF. However, SoMix relied on an ED to stabilize the TDO against frequency pulling. The RTO instead stabilizes oscillation using the high-Q SAW resonator, enabling standalone reception. We characterize autodyning using the cabled setup in Figure 15(a), where the RTO connects to a Mini-Circuits ZN2PD2-63-S+ power combiner [59]. An RF signal from a USRP SDR is injected into one port and the downconverted IF signal is observed with a spectrum analyzer. We sweep the frequency offset from 50 kHz to 10 MHz while varying input power. Figure 15(b) shows the RTO successfully downconverts across the tested range.

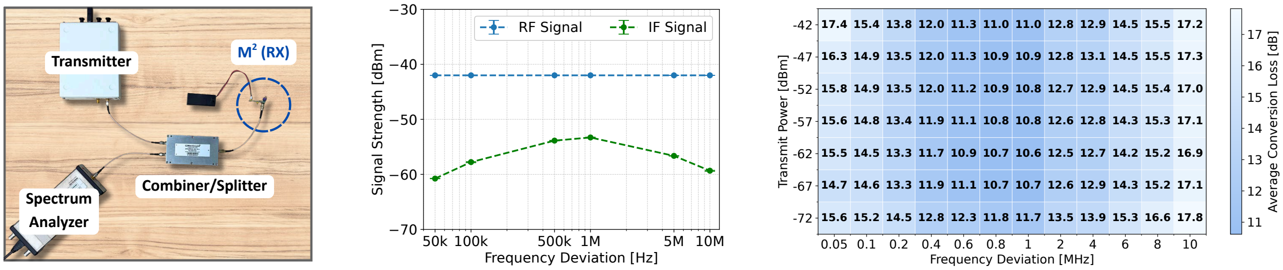

(a) Experiment Setup (b) Varying Frequency Deviation (c) Conversion Loss

Figure 15: The RTO downconverts incoming signals to IF via autodyning, with conversion loss below 17.8 dB **across the tested range. This is substantially lower than the classical TDO, achieved at only modest SAW-resonator power overhead, translating to longer reception range.**

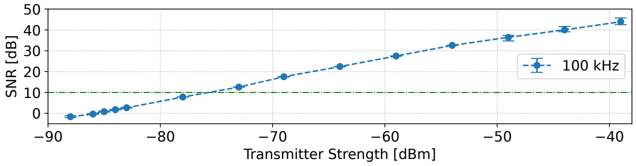

Figure 16: M^2 receives and downconverts signals as weak as −75 dBm **while maintaining a minimum SNR of** 10 dB**, with the incoming signal swept at a fixed** 100 kHz **offset from the carrier. Relaxing this threshold enables reception of weaker signals, surpassing the sensitivity of SoTA low-power receivers.**

To quantify downconversion efficiency, we compute conversion loss at each operating point, averaged over three runs. The heatmap in Figure 15(c) shows conversion loss ranging from 10.6 dB to 17.8 dB. The consistent values across input power levels indicate that the RTO maintains stable downconversion over a wide dynamic range. Compared with the 25 dB to 30 dB conversion loss reported by SoMix [58], the RTO achieves substantially lower loss, with an improvement of approximately 14 dB at its best operating point. These results confirm that the RTO preserves efficient autodyne downconversion while eliminating the need for an external carrier. The improved sensitivity translates to longer reception range.

Sensitivity. Sensitivity determines the reception range. We evaluate M^2's sensitivity using the same cabled setup for the autodyning characterization, measuring the SNR of the downconverted IF signal as a function of input RF power at a fixed frequency offset of 100 kHz. Input power is swept from −90 dBm to −40 dBm. Figure 16 shows the measured SNR response, which exhibits a linear relationship with received signal strength. At a 10 dB SNR threshold, typically sufficient for reliable demodulation of simple modulation schemes such as OOK, the frontend maintains SNR above threshold for inputs as weak as −75 dBm. This surpasses SoMix [58], which reports −70 dBm sensitivity. M^2 improves sensitivity by 5 dB and eliminates the ED, enabling a low-power standalone receiver.

4 Evaluation

We evaluate M^2 in two environments. The first is an outdoor line-of-sight (LoS) setting in a building basement opening to a road, as shown in Figure 17(a). The second is an indoor non-line-of-sight (NLoS) setting with multiple offices separated by concrete walls, as shown in Figure 21(a). Spectral measurements use Signal Hound BB60C/BB60D[36, 84] spectrum analyzers, transmission experiments use a custom 2-FSK transmitter with a TI CC1310[95] receiver, and autodyning reception experiments use a USRP B200 SDR[23] as the transmitter. Packets consist of a 4-byte preamble, 4-byte synchronization word, 1-byte sequence number, 1-byte node identifier, and 14-byte payload, with the cyclic redundancy check disabled to enable the capture and analysis of corrupted packets.

System	Phase Noise (dBc/Hz)						
	10 Hz	100 Hz	1 kHz	10 kHz	100 kHz	1 MHz	10 MHz
Conventional Injection locked TDO	-54.75	-64.04	-81.56	-88.94	-98.88	-116.90	-118.49
Commercial SDR	-62.80	-78.61	-87.07	-92.43	-99.05	-117.38	-118.75
M^2 (over the air)	-21.46	-44.43	-80.83	-92.30	-99.01	-109.93	-108.89
M^2	**-29.92**	**-62.23**	**-83.08**	**-92.25**	**-99.29**	**-119.02**	**-118.82**

Table 4: The carrier generated by M^2 exhibits phase-noise performance comparable to that of a commercial SDR and a conventional injection-locked TDO.

4.1 Phase Noise

We evaluate M^2's phase noise and compare it with that of an injection-locked TDO and a commercial SDR. We connect the RTO to a BB60C spectrum analyzer via a coaxial cable and use its built-in phase-noise measurement function to evaluate phase noise at different frequency offsets, as shown in Table 4. The setup is kept in an isolated room to reduce the impact of the environment on measurements. At close-in offsets (10–100 Hz), M^2 exhibits slightly higher phase noise than the injection-locked reference, as expected for a free-running oscillator. Beyond a 1 kHz offset, however, M^2 phase noise closely matches that of both the commercial SDR and the injection-locked TDO. Overall, M^2 achieves SDR-like spectral purity at practically relevant offsets, enabling reliable communication.

4.2 Communication Range

A key question is whether M^2's improved carrier signal frequency stability translates into a better link budget. We evaluate communication range in both outdoor LoS and indoor NLoS settings.

Transmission range. In the outdoor LoS setting, the transmitter generates a 434 MHz carrier at −17.5 dBm, and we measure received SNR at increasing distance using a spectrum analyzer. As shown in Figure 17(b), the signal remains detectable with SNR above 3 dB up to 135 m, demonstrating that the M^2 frontend supports long-range transmissions. In a complex indoor NLoS environment with multiple rooms separated by concrete walls and floors, Figure 18(b) shows the signal remains above 5 dB SNR up to 46 m despite challenging propagation. Together, these results show that M^2 provides sufficient link budget for practical ranges of tens of meters in obstructed indoor settings and over 100 m in outdoor LoS. The measured SNR levels also indicate headroom for higher-bitrate communication at shorter ranges, which we demonstrate in the following experiments.

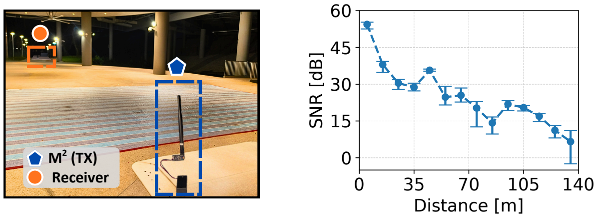

(a) Experiment Setup (b) Link Metrics (SNR)

Figure 17: M² achieves outdoor line-of-sight transmission up to 135 m **with an active CC1310 receiver. Buildings on one side introduce multipath reflections.**

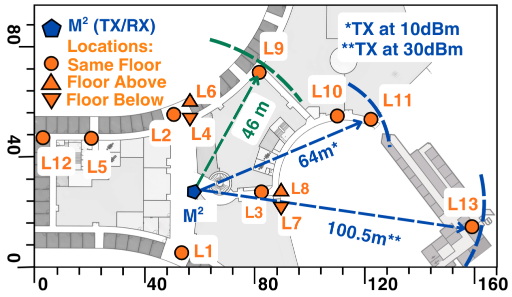

(a) Floor Plan of the Indoor NLoS Evaluation Environment

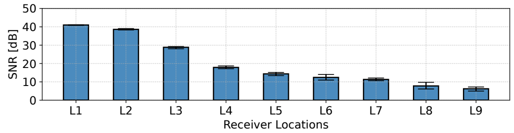

(b) Transmission SNR across Locations

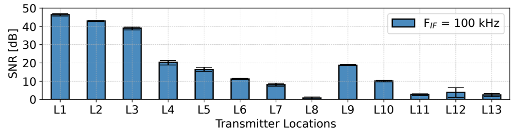

(c) Reception SNR across Locations

Figure 18: M² supports transmission and reception across a complex indoor NLoS environment with multiple concrete walls. The transmitter maintains SNR above 5 dB **up to** 46 m**, while the receiver captures signals up to** 64 m.

Reception range. M² enables low-power reception through autodyning. We evaluate reception range in the same indoor NLoS environment, with a USRP B200 transmitting at 10 dBm (regulatory limit for maximum strength transmissions at our location) and the M² receiver kept at a fixed location. The downconverted IF signal at 100 kHz is monitored via a spectrum analyzer. As shown in Figures 18(a) and 18(c), M² detects signals from up to 64 m through multiple concrete walls, extending beyond 100 m (Location 13) when transmit power is increased to 30 dBm. Compared to SoMix [58], which reports 54 m indoor NLoS range at 868 MHz and 30 dBm, M² achieves longer range at 20 dB lower transmit power. While 433 MHz provides an approximate 6 dB free-space advantage over 868 MHz, this alone does not account for the reception range improvement. We attribute the remaining advantage to lower conversion loss, higher sensitivity, and improved carrier stability. These results highlight M²'s potential for practical deployments by enabling low-power reception without a dedicated ED.

Symmetric M²-to-M² range. M² enables low-power tag-to-tag communication. We evaluate a fully symmetric end-to-end link in which both nodes use a M² transceiver, operating at 433 MHz with an intermediate frequency of 200 kHz. We conduct the experiment in a complex indoor environment, a challenging setting where state-of-the-art solutions achieve only a few meters of range at low bitrates [69, 79]. We gradually increase separation between the two M² nodes and record the SNR of the downconverted IF signal at the receiver. Figure 19 shows that received SNR decreases gradually with distance, remaining observable up to 40 m. This demonstrates the potential for tag-to-tag communication using M² without an active transceiver or ED. These results indicate that M² can help realize the long-standing vision of ambient backscatter [50].

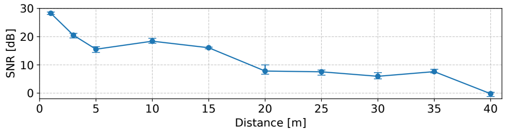

Figure 19: Two M² nodes achieve reliable tag-to-tag communication up to 40 m **in a complex indoor environment.**

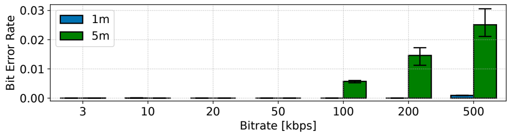

Figure 20: M² supports reliable communication up to 500 kbps **with near-zero BER at short range. The maximum tested rate is limited by the CC1310 receiver, not M². Higher bitrates are achievable with a wideband receiver.**

4.3 Communication Reliability

We next evaluate the reliability of communication enabled by M² across bitrate, distance, and deployment scenarios.

Supported transmission bitrate. We evaluate the bitrate supported by the M² transmitter by generating 2-FSK signals carrying pseudorandom payloads at bitrates from 3 kbps to 500 kbps. The pseudorandom payload prevents bias in errors. For each rate, we scale frequency deviation proportionally and collect 6,000 packets across three runs using a CC1310 receiver at 1 m and 5 m. We limit this study to 500 kbps, the maximum 2-FSK bitrate the CC1310 supports. The M² transmitter can likely support higher bitrates, as Figure 14 shows successful SoM at larger baseband frequencies. Figure 20 shows that at 1 m, BER remains near zero up to 200 kbps, indicating a highly stable short-range link; even at 500 kbps, BER is only 0.0009. At 5 m, BER begins rising beyond 100 kbps, reaching approximately 0.017 at 200 kbps and 0.03 at 500 kbps. These BER values are significantly better than those of related systems [65, 70, 100, 103], a direct consequence of the RTO's exceptional stability.

Transmission bit error-rate. We evaluate the reliability of M² transmissions (measured through bit error-rate) in a complex NLoS environment with multiple rooms separated by thick concrete walls, as shown in Figure 21, using 2-FSK modulation. We focus on this for brevity as it is a challenging environment. We conduct two experiments, with the first at 3 kbps bitrate with a subcarrier offset of 90 kHz and frequency deviation of 10 kHz; the second at 100 kbps with a subcarrier offset of 844.44 kHz and frequency deviation of 44.44 kHz. These configurations support a range of practical scenarios. Furthermore, owing to their small frequency deviations, they enable concurrent transmissions from multiple nodes via Frequency Division Multiple Access (FDMA), as we demonstrate in Section 4.4. We place the M² transmitter in one room and collect 1,000 packets across three runs at each receiver location in subsequent rooms.

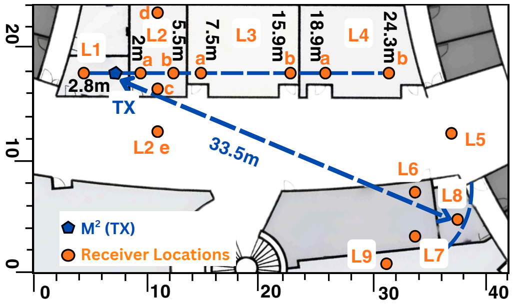

(a) Floor Plan of the Indoor NLoS Experiment

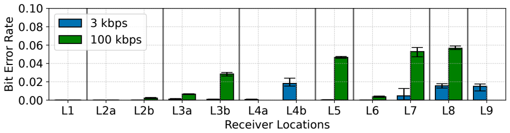

(b) BER at Varying Bitrates

Figure 21: M² enables NLoS transmission through multiple concrete walls and metallic beams, with reliable reception up to 33.5 m across tested bitrates.

Figure 21 shows a maximum range of about 33.5 m across both bitrates, with peak BER reaching 0.023 for 3 kbps (L4b) and 0.057 for 100 kbps (L8). Given the complex environment and distances involved, communication remains reliable for practical embedded deployments. We also estimate the bitrate supported by the M² receiver using theoretical calculations as detailed in Figure 24 and Appendix B, showing support for bitrates over 10 kbps at a 10^{-3} BER threshold at distances up to 50 m in this NLoS environment.

M² as an emitter device. We evaluate whether M² can serve as a low-power ED for backscatter systems. We place M² at a fixed position and measure SNR and BER from a 2-FSK backscatter tag at varying distances (details in Appendix C). As shown in Figure 25, M² can support legacy tags, reducing the need for dedicated ED.

Adjacent channel interference. We evaluate the M² receiver's reliability to adjacent channel interference. A USRP B210 transmitter 3 m away generates the desired signal at a fixed 200 kHz offset from the RTO frequency, reflecting practical deployments where an interferer may occupy an adjacent channel. A second co-located USRP generates the interfering signal, sweeping its frequency offset and power to vary the interferer-to-signal ratio (ISR). Figure 22 shows degradation within a few decibels relative to the interference-free baseline, with no measurable dependence on ISR or interferer offset. However, when the interferer is both strong and spectrally close to the RTO frequency, the RTO exhibits injection pulling or locking, occurring at an ISR of 30 dB for offsets up to 300 kHz. These results confirm that the M² frontend rejects most adjacent channel interference, failing only under high-power interferers within the RTO's locking range, a scenario unlikely in deployments.

4.4 Multi-User Communication

We demonstrate multi-user communication by operating three M² transmitters concurrently in the indoor environment of Figure 18(a). The transmitters (TX1, TX2, TX3) are co-located 1 m apart between L2a and L2b, all tuned to the 433 MHz band. We adopt FDMA, allocating each transmitter a distinct channel, as shown in Figure 23(a). Each transmitter is modulated with a 2-FSK baseband signal at sub-carrier offsets of 844.44 kHz, 1.071 MHz, and 1.071 MHz, respectively; the last two transmitters use RTOs with slightly different center frequencies, ensuring distinct channels despite the identical offsets. All three communicate at a bitrate of 10 kbps. A CC1310 receiver collects 1000 packets across three runs at each location. Figure 23(b) shows the results. All three transmissions are received concurrently with BER remaining near zero, rising only at farther locations due to signal degradation. Although the SAW resonator fixes the RTO frequency, the SoM property allows each transmitter to place its modulated signal at a different IF offset, effectively creating distinct channels. To change the RTO frequency, SAW resonators of different resonant frequencies could be used.

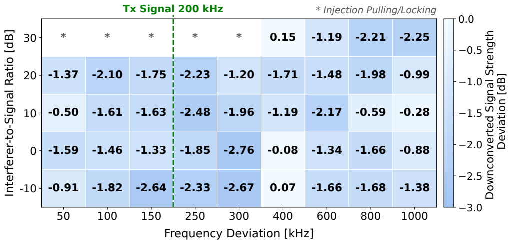

	50	100	150	250	300	400	600	800	1000
30	*	*	*	*	*	0.15	-1.19	-2.21	-2.25
20	-1.37	-2.10	-1.75	-2.23	-1.20	-1.71	-1.48	-1.98	-0.99
10	-0.50	-1.61	-1.63	-2.48	-1.96	-1.19	-2.17	-0.59	-0.28
0	-1.59	-1.46	-1.33	-1.85	-2.76	-0.08	-1.34	-1.66	-0.88
-10	-0.91	-1.82	-2.64	-2.33	-2.67	0.07	-1.66	-1.68	-1.38

Figure 22: M² receiver maintains stable downconversion across most interferer power levels and frequency offsets, with IF signal degradation occurring only when a strong interferer falls within the RTO's locking range.

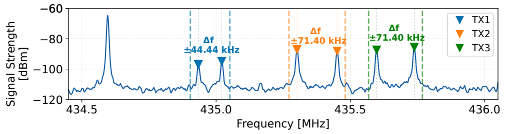

(a) Combined Spectrum of Three Concurrent Transmitters

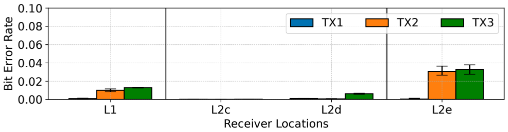

(b) BER across Indoor NLoS Environment Locations

Figure 23: Three co-located M² transmitters simultaneously modulate independent transmissons on distinct frequency channels, demonstrating FDMA operation without mutual interference at multiple indoor NLoS locations.

5 Conclusion

We presented M², which breaks the power-stability tradeoff in oscillator design by generating a carrier at 105 µW with stability below 2.10 ppm. M² also exhibits self-oscillating mixing and autodyning, enabling transmission and reception over tens of meters indoors. In deployments such as a university food court, M² maintains drift under 35 ppm. We further show tag-to-tag link up to 40 m. M² takes a concrete step toward eliminating the delegation architecture that has constrained embedded systems for over a decade.

6 Acknowledgements

We thank the anonymous reviewers and our shepherd for their feedback. This work was funded by a Tier-1 grant from the Ministry of Education (A-8001661-00-00), a startup grant from ODPRT (A-8000277-00-00), and an unrestricted gift from Google through the Google Research Scholar Program (A-8002307-00-00-00), all hosted at the National University of Singapore. This work was also supported in part by an Okawa Foundation Research Grant and DENSO International America, Inc., awarded to Prof. Prabal Dutta and hosted at the University of California, Berkeley.

References

[1] Ablic Inc. 2019. S-1313 Series: Small Package Low-Dropout CMOS Voltage Regulator. Datasheet. https://www.ablic.com/en/doc/datasheet/voltage_regulator/S1313_E.pdf [Accessed: 2026-03-20].

[2] Francesco Amato. 2017. *Achieving hundreds-meter ranges in low powered RFID systems with quantum tunneling tags.* Ph. D. Dissertation. Georgia Institute of Technology. http://hdl.handle.net/1853/58228

[3] Francesco Amato, Hakki M. Torun, and Gregory D. Durgin. 2018. RFID Backscattering in Long-Range Scenarios. *IEEE Transactions on Wireless Communications* 17, 4 (2018), 2718–2725. doi:10.1109/TWC.2018.2801803

[4] Nivedita Arora, Steven L. Zhang, Fereshteh Shahmiri, Diego Osorio, Yi-Cheng Wang, Mohit Gupta, Zhengjun Wang, Thad Starner, Zhong Lin Wang, and Gregory D. Abowd. 2018. SATURN: A Thin and Flexible Self-powered Microphone Leveraging Triboelectric Nanogenerator. *Proc. ACM Interact. Mob. Wearable Ubiquitous Technol.* 2, 2, Article 60 (July 2018), 28 pages. doi:10.1145/3214263

[5] Kang Min Bae, Namjo Ahn, Yoon Chae, Parth Pathak, Sung-Min Sohn, and Song Min Kim. 2022. OmniScatter: extreme sensitivity mmWave backscattering using commodity FMCW radar. In *Proceedings of the 20th Annual International Conference on Mobile Systems, Applications and Services* (Portland, Oregon) *(MobiSys '22)*. Association for Computing Machinery, New York, NY, USA, 316–329. doi:10.1145/3498361.3538924

[6] David C. Burnett, Filip Maksimovic, Brad Wheeler, Osama Khan, Ali M. Niknejad, and Kristofer S.J. Pister. 2021. Free-running 2.4GHz Ring Oscillator-Based FSK TX/RX for Ultra-Small IoT Motes. In *2020 15th European Microwave Integrated Circuits Conference (EuMIC)*. 101–104.

[7] David C. Burnett, Brad Wheeler, Filip Maksimovic, Osama Khan, Ali M. Niknejad, and Kristofer S.J. Pister. 2017. Narrowband communication with free-running 2.4GHz ring oscillators. In *2017 International Conference on Performance Evaluation and Modeling in Wired and Wireless Networks (PEMWN)*. 1–6. doi:10.23919/PEMWN.2017.8308023

[8] Sheng-Kai Chang, Zhi-Wei Lin, and Kuang-Wei Cheng. 2024. A Multichannel Injection-Locked OOK Transmitter With Current Mode Edge-Combining Power Amplifier. *IEEE Solid-State Circuits Letters* 7 (2024), 111–114. doi:10.1109/LSSC.2024.3375329

[9] Kameswari Chebrolu, Bhaskaran Raman, Nilesh Mishra, Phani Kumar Valiveti, and Raj Kumar. 2008. Brimon: a sensor network system for railway bridge monitoring. In *Proceedings of the 6th International Conference on Mobile Systems, Applications, and Services* (Breckenridge, CO, USA) *(MobiSys '08)*. Association for Computing Machinery, New York, NY, USA, 2–14. doi:10.1145/1378600.1378603

[10] Kuang-Wei Cheng, Sheng-Kai Chang, Shao-Ting Chang, Si-Lou Li, and Yu-Chieh Huang. 2023. An 11 pJ/Bit Multichannel OOK/FSK/QPSK Transmitter With Multi-Phase Injection-Locking and Frequency Multiplication Techniques. *IEEE Transactions on Circuits and Systems I: Regular Papers* 70, 12 (2023), 5229–5241. doi:10.1109/TCSI.2023.3321917

[11] R. B. Clover and W. P. Wolf. 1970. Magnetic Susceptibility Measurements with a Tunnel Diode Oscillator. *Rev. Sci. Instrum.* 41, 5 (1970), 617–621. doi:10.1063/1.1684598

[12] Digilent. 2023. Analog Discovery 3: 125 MS/s USB Oscilloscope, Waveform Generator, Logic Analyzer, and Variable Power Supply. Datasheet. https://files.digilent.com/datasheets/Analog-Discovery-3-Datasheet.pdf [Accessed: 2025-11-20].

[13] Huixin Dong, Liu Yang, Lehuan Yang, Zhiqing Luo, Chunshen li, Xianan Zhang, and Wei Wang. 2024. A Unified Tunnel-diode Based Low Power Signal Waveform Transform Hardware for RF Computing. In *Proceedings of the First International Workshop on Radio Frequency (RF) Computing* (Hangzhou, China) *(RFCom '24)*. Association for Computing Machinery, New York, NY, USA, 36–37.

[14] Manideep Dunna, Miao Meng, Po-Han Wang, Chi Zhang, Patrick Mercier, and Dinesh Bharadia. 2021. SyncScatter: Enabling WiFi like synchronization and range for WiFi backscatter Communication. In *18th USENIX Symposium on Networked Systems Design and Implementation (NSDI 21)*. USENIX Association, 923–937. https://www.usenix.org/conference/nsdi21/presentation/dunna

[15] Prabal Dutta, Stephen Dawson-Haggerty, Yin Chen, Chieh-Jan Mike Liang, and Andreas Terzis. 2012. A-MAC: A versatile and efficient receiver-initiated link layer for low-power wireless. *ACM Trans. Sen. Netw.* 8, 4, Article 30 (sep 2012), 29 pages. doi:10.1145/2240116.2240119

[16] Y. Ebata, Koji Sato, and Shigefumi Morishita. 1981. A LiTaO 3 SAW resonator and its application to video cassette recorder. In *1981 Ultrasonics Symposium*. IEEE, 111–116.

[17] Aline Eid, Jimmy Hester, and Manos M. Tentzeris. 2020. A 5.8 GHz Fully-Tunnel-Diodes-Based 20 µW, 88mV, and 48 dB-Gain Fully-Passive Backscattering RFID Tag. In *2020 IEEE/MTT-S International Microwave Symposium (IMS)*. 607–610. doi:10.1109/IMS30576.2020.9224116

[18] General Electric. 2023. 1N3712 Germanium Tunnel Diode Technical Specifications. http://w140.com/tekwiki/wiki/1N3712 [Accessed: 2025-08-10].

[19] Joshua F. Ensworth, Alexander T. Hoang, and Matthew S. Reynolds. 2017. A low power 2.4 GHz superheterodyne receiver architecture with external LO for wirelessly powered backscatter tags and sensors. In *2017 IEEE International Conference on RFID (RFID)*. 149–154. doi:10.1109/RFID.2017.7945601

[20] Joshua F. Ensworth and Matthew S. Reynolds. 2017. BLE-Backscatter: Ultralow-Power IoT Nodes Compatible With Bluetooth 4.0 Low Energy (BLE) Smartphones and Tablets. *IEEE Transactions on Microwave Theory and Techniques* 65, 9 (2017), 3360–3368. doi:10.1109/TMTT.2017.2687866

[21] Leo Esaki. 1958. New phenomenon in narrow germanium p- n junctions. *Physical review* 109, 2 (1958), 603.

[22] Leo Esaki. 1980. Tunnel Diode. U.S. Patent 4,198,644. Filed June 9, 1978. Assignee: United States Department of the Army.

[23] Ettus Research. 2019. USRP B200/B210 Product Specification. Specification Sheet. https://www.ettus.com/wp-content/uploads/2019/01/b200-b210_spec_sheet.pdf [Accessed: 2025-11-20].

[24] Reona Ezaki and Yuriko Kurose. 1962. Diode Type Semiconductor Device. U.S. Patent 3,033,714. Filed May 8, 1958. Priority: Japan, Sept. 28, 1957. Assignee: Sony Corporation.

[25] Ander Galisteo, Ambuj Varshney, and Domenico Giustiniano. 2020. Two to tango: hybrid light and backscatter networks for next billion devices. In *Proceedings of the 18th International Conference on Mobile Systems, Applications, and Services* (Toronto, Ontario, Canada) *(MobiSys '20)*. Association for Computing Machinery, New York, NY, USA, 80–93. doi:10.1145/3386901.3388918

[26] Nakul Garg and Nirupam Roy. 2023. Sirius: A Self-Localization System for Resource-Constrained IoT Sensors. In *Proceedings of the 21st Annual International Conference on Mobile Systems, Applications and Services* (Helsinki, Finland) *(MobiSys '23)*. Association for Computing Machinery, New York, NY, USA, 289–302. doi:10.1145/3581791.3596861

[27] Sylvester P. Gentile. 1962. *Basic Theory and Application of Tunnel Diodes.* D Van Nostrand Company Inc.

[28] Alexander Glas. 2001. *Application Note: SAW-Components—Principles of SAWR-Stabilized Oscillators and Transmitters (Version 2.1).* EPCOS AG, Munich, Germany. https://jap.hu/electronic/rf/434MHz_SAW-based_oscillators_and_transmitters.pdf [Accessed: 2025-11-12].

[29] Jeremy Gummeson, Shane S. Clark, Kevin Fu, and Deepak Ganesan. 2010. On the Limits of Effective Hybrid Micro-Energy Harvesting on Mobile CRFID Sensors. In *Proceedings of the 8th International Conference on Mobile Systems, Applications, and Services* (San Francisco, California, USA) *(MobiSys '10)*. Association for Computing Machinery, New York, NY, USA, 195–208. doi:10.1145/1814433.1814454

[30] Xiuzhen Guo, Yuan He, Jing Nan, Jiacheng Zhang, Yunhao Liu, and Longfei Shangguan. 2024. A Low-Power Demodulator for LoRa Backscatter Systems With Frequency-Amplitude Transformation. *IEEE/ACM Trans. Netw.* 32, 4 (May 2024), 3515–3527. doi:10.1109/TNET.2024.3396509

[31] Xiuzhen Guo, Boya Liu, Nan Jing, Chaojie Gu, Yuanchao Shu, and Jiming Chen. 2025. Enabling Cross-Band Backscatter Communication With Twaltz. *IEEE Transactions on Mobile Computing* 24, 11 (2025), 11323–11336. doi:10.1109/TMC.2025.3581900

[32] Xiuzhen Guo, Longfei Shangguan, Yuan He, Nan Jing, Jiacheng Zhang, Haotian Jiang, and Yunhao Liu. 2022. Saiyan: Design and Implementation of a Low-power Demodulator for LoRa Backscatter Systems. In *19th USENIX Symposium on Networked Systems Design and Implementation (NSDI 22)*. USENIX Association, Renton, WA, 437–451.

[33] Mehrdad Hessar, Ali Najafi, and Shyamnath Gollakota. 2019. Netscatter: enabling large-scale backscatter networks. In *Proceedings of the 16th USENIX Conference on Networked Systems Design and Implementation* (Boston, MA, USA) *(NSDI'19)*. USENIX Association, USA, 271–283.

[34] M. E. Hines. 1960. High-Frequency Negative-Resistance Circuit Principles for Esaki Diode Applications. *Bell Syst. Tech. J.* 39 (1960), 477–513. doi:10.1002/j.1538-7305.1960.tb03933.x

[35] P. T. Ho. 1982. Ku-Band Tunnel Diode Amplifier for the INTELSAT-V Communication Satellites. In *IEEE MTT-S Int. Microwave Symp. Dig.* Ford Aerospace & Communications Corp., 601–608.

[36] Signal Hound. 2023. BB60C Signal Analyzer. https://signalhound.com/sigdownloads/datasheets/Signal-Hound-BB60C-Data-Sheet.pdf. [Accessed: 2025-11-20].

[37] O. Ikata, T. Miyashita, T. Matsuda, T. Nishihara, and Y. Satoh. 1992. Development of low-loss band-pass filters using SAW resonators for portable telephones. In *IEEE 1992 Ultrasonics Symposium Proceedings*. IEEE, 111–115.

[38] Vikram Iyer, Vamsi Talla, Bryce Kellogg, Shyamnath Gollakota, and Joshua Smith. 2016. Inter-Technology Backscatter: Towards Internet Connectivity for Implanted Devices. In *Proceedings of the 2016 ACM SIGCOMM Conference* (Florianopolis, Brazil) *(SIGCOMM '16)*. Association for Computing Machinery, New York, NY, USA, 356–369. doi:10.1145/2934872.2934894

[39] Jinyan Jiang, Zhenqiang Xu, Fan Dang, and Jiliang Wang. 2021. Long-range ambient LoRa backscatter with parallel decoding. In *Proceedings of the 27th Annual International Conference on Mobile Computing and Networking* (New Orleans, Louisiana) *(MobiCom '21)*. Association for Computing Machinery, New York, NY, USA, 684–696. doi:10.1145/3447993.3483261

[40] Oh-Yong Jung, Hyun-Gi Seok, Anjana Dissanayake, and Sang-Gug Lee. 2018. A 45- μ W, 162.1-dBc/Hz FoM, 490-MHz Two-Stage Differential Ring VCO Without a Cross-Coupled Latch. *IEEE Transactions on Circuits and Systems II: Express*

Briefs 65, 11 (2018), 1579–1583. doi:10.1109/TCSII.2017.2766674

[41] J. M. Kahn, R. H. Katz, and K. S. J. Pister. 1999. Next century challenges: mobile networking for "Smart Dust". In *Proceedings of the 5th Annual ACM/IEEE International Conference on Mobile Computing and Networking* (Seattle, Washington, USA) *(MobiCom '99)*. Association for Computing Machinery, New York, NY, USA, 271–278. doi:10.1145/313451.313558

[42] Bryce Kellogg, Vamsi Talla, Shyamnath Gollakota, and Joshua R. Smith. 2016. Passive Wi-Fi: Bringing Low Power to Wi-Fi Transmissions. In *Proceedings of the 13th Usenix Conference on Networked Systems Design and Implementation* (Santa Clara, CA) *(NSDI'16)*. USENIX Association.

[43] Keysight Technologies. 2017. B2900A Series Precision Source/Measure Unit (SMU) Data Sheet. https://www.keysight.com/us/en/assets/7018-02717/data-sheets/5990-7009.pdf. [Accessed: 2026-03-20].

[44] C. S. Kim and A. Brändli. 1961. High-Frequency High-Power Operation of Tunnel Diodes. *IRE Transactions on Circuit Theory* 8, 4 (Dec. 1961), 416–425. doi:10.1109/TCT.1961.1086849

[45] Sung-Geun Kim, Jinsoo Rhim, Dae-Hyun Kwon, Min-Hyeong Kim, and Woo-Young Choi. 2016. A Low-Voltage PLL With a Supply-Noise Compensated Feedforward Ring VCO. *IEEE Transactions on Circuits and Systems II: Express Briefs* 63, 6 (2016), 548–552. doi:10.1109/TCSII.2016.2531199

[46] John Kimionis, Manos M. Tentzeris, Apostolos Georgiadis, and Ana Collado. 2014. Inkjet-printed reflection amplifier for increased-range Backscatter radio. In *2014 44th European Microwave Conference*. 5–8. doi:10.1109/EuMC.2014.6986355

[47] Eric A. Kittlaus, William M. Jones, Peter T. Rakich, Nils T. Otterstrom, Richard E. Muller, and Mina Rais-Zadeh. 2021. Electrically Driven Acousto-Optics and Broadband Non-Reciprocity in Silicon Photonics. *Nature Photonics* 15 (2021), 43–52. doi:10.1038/s41566-020-00711-9

[48] Songfan Li, Hui Zheng, Chong Zhang, Yihang Song, Shen Yang, Minghua Chen, Li Lu, and Mo Li. 2022. Passive DSSS: Empowering the Downlink Communication for Backscatter Systems. In *19th USENIX Symposium on Networked Systems Design and Implementation (NSDI 22)*. USENIX Association, Renton, WA, 913–928.

[49] Chung-Ching Lin, Huan Hu, and Subhanshu Gupta. 2021. Improved Performance Tradeoffs in Harmonic Injection-Locked ULP TX for Sub-GHz Radios. *IEEE Transactions on Microwave Theory and Techniques* 69, 6 (2021), 2885–2898. doi:10.1109/TMTT.2021.3064056

[50] Vincent Liu, Aaron Parks, Vamsi Talla, Shyamnath Gollakota, David Wetherall, and Joshua R. Smith. 2013. Ambient Backscatter: Wireless Communication out of Thin Air. In *Proceedings of the ACM SIGCOMM 2013 Conference on SIGCOMM* (Hong Kong, China) *(SIGCOMM '13)*. Association for Computing Machinery, New York, NY, USA, 39–50. doi:10.1145/2486001.2486015

[51] Alan Mainwaring, David Culler, Joseph Polastre, Robert Szewczyk, and John Anderson. 2002. Wireless sensor networks for habitat monitoring. In *Proceedings of the 1st ACM International Workshop on Wireless Sensor Networks and Applications* (Atlanta, Georgia, USA) *(WSNA '02)*. Association for Computing Machinery, New York, NY, USA, 88–97. doi:10.1145/570738.570751

[52] Amjad Yousef Majid, Michel Jansen, Guillermo Ortas Delgado, Kasim Sinan Yildirim, and Przemysław Pawełczak. 2019. Multi-hop Backscatter Tag-to-Tag Networks. In *IEEE INFOCOM 2019 - IEEE Conference on Computer Communications*. 721–729. doi:10.1109/INFOCOM.2019.8737551

[53] Filip Maksimovic, Brad Wheeler, David C. Burnett, Osama Khan, Sahar Mesri, Ioana Suciu, Lydia Lee, Alex Moreno, Arvind Sundararajan, Bob Zhou, Rachel Zoll, Andrew Ng, Tengfei Chang, Xavier Villajosana, Thomas Watteyne, Ali Niknejad, and Kristofer S. J. Pister. 2019. A Crystal-Free Single-Chip Micro Mote with Integrated 802.15.4 Compatible Transceiver, sub-mW BLE Compatible Beacon Transmitter, and Cortex M0. In *2019 Symposium on VLSI Circuits*. C88–C89. doi:10.23919/VLSIC.2019.8777971

[54] P. Massoud Salehi and J. Proakis. 2007. *Digital Communications*. McGraw-Hill Education. https://books.google.com.sg/books?id=HroiQAAACAAJ [Accessed: 2025-11-20].

[55] Maxim Integrated (now Analog Devices, Inc.) 2020. *MAX2750/MAX2751/MAX2752: 2.4 GHz Monolithic Voltage-Controlled Oscillators*. Maxim Integrated (now Analog Devices, Inc.). https://www.analog.com/media/en/technical-documentation/data-sheets/max2750-max2752.pdf Rev. 1, 19-1825; 05/2012; [Accessed: 2025-11-20].

[56] Maxim Integrated (now Analog Devices, Inc.) 2025. *MAX2605–MAX2609: 45 MHz to 650 MHz, Integrated IF VCOs with Differential Output; Rev. 0a*. Maxim Integrated (now Analog Devices, Inc.). https://www.analog.com/media/en/technical-documentation/data-sheets/max2605-max2609.pdf [Accessed: 2025-11-12].

[57] Maxim Integrated (now Analog Devices, Inc.) 2026. *MAX2622/MAX2623/MAX2624: Monolithic Voltage-Controlled Oscillators*. Maxim Integrated (now Analog Devices, Inc.). https://www.analog.com/media/en/technical-documentation/data-sheets/MAX2622-MAX2624.pdf 19-1528; Rev 1; 5/00; [Accessed: 2025-11-20].

[58] Sooriya Patabandige Pramuka Medaranga, Rajashekar Reddy Chinthalapani, Wenqing Yan, Prabal Dutta, and Ambuj Varshney. 2025. Unraveling the Missing Link in Low-power Communication: An Autodyning Receiver Architecture that Achieves a Long Range. In *Proceedings of the 23rd Annual International Conference on Mobile Systems, Applications and Services* (Anaheim, CA, USA) *(MobiSys '25)*. Association for Computing Machinery, New York, NY, USA, To Appear. doi:10.1145/3711875.3729164

[59] Mini-Circuits. 2020. ZN2PD2-63-S+: 2-Way-0° Power Splitter, DC–6000 MHz, 50 Ω. Datasheet. https://www.minicircuits.com/pdfs/ZN2PD2-63-S+.pdf [Accessed: 2025-11-20].

[60] Muhammad Sarmad Mir, Wenqing Yan, Prabal Dutta, Domenico Giustiniano, and Ambuj Varshney. 2023. TunnelLiFi: Bringing LiFi to Commodity Internet of Things Devices. In *Proceedings of the 24th International Workshop on Mobile Computing Systems and Applications* (Newport Beach, California) *(HotMobile '23)*. Association for Computing Machinery, New York, NY, USA, 1–7. doi:10.1145/3572864.3580327

[61] G. T. Munsterman. 1965. Tunnel-Diode Microwave Amplifiers. *APL Technical Digest* 4, 5 (1965), 2–9.

[62] Murata Manufacturing Co., Ltd. 2002. *SAW Resonators (SARCC Series): Applications and Actual Measurements of SAW Oscillator*. Murata Manufacturing Co., Ltd. https://www.farnell.com/datasheets/573768.pdf Cat.No. P36E, includes 315 MHz and 433.92 MHz oscillator measurement data; [Accessed: 2025-11-20].

[63] Saman Naderiparizi, Mehrdad Hessar, Vamsi Talla, Shyamnath Gollakota, and Joshua R Smith. 2018. Towards Battery-Free HD Video Streaming. In *15th USENIX Symposium on Networked Systems Design and Implementation (NSDI 18)*. USENIX Association, Renton, WA.

[64] Saman Naderiparizi, Aaron N. Parks, Zerina Kapetanovic, Benjamin Ransford, and Joshua R. Smith. 2015. WISPCam: A battery-free RFID camera. In *2015 IEEE International Conference on RFID (RFID)*. 166–173. doi:10.1109/RFID.2015.7113088

[65] Madhushanka Padmal. 2025. *Wireless Communication Systems for Energy-Constrained Environments*. Ph. D. Dissertation. Uppsala University, Uppsala, Sweden. https://urn.kb.se/resolve?urn=urn:nbn:se:uu:diva-565283

[66] Madhushanka Padmal, Dilushi Piumwardane, and Thiemo Voigt. 2026. SharpPeak: Unlocking the True Potential of Tunnel Diodes for Low-Power Long-Range Communication. In *Proceedings of the 24th ACM Conference on Embedded Networked Sensor Systems (SenSys '26)*. Association for Computing Machinery, New York, NY, USA.

[67] T.E. Parker. 1982. Development of precision SAW oscillators for military applications. In *Proc. 36th Ann. Symp. on Frequency Control*. 453–458.

[68] T. E. Parker and G. K. Montress. 1988. Precision Surface-Acoustic-Wave (SAW) Oscillators. *IEEE Trans. Ultrason. Ferroelectr. Freq. Control* 35, 3 (1988), 342–364.

[69] Aaron N. Parks, Angli Liu, Shyamnath Gollakota, and Joshua R. Smith. 2014. Turbocharging ambient backscatter communication. *SIGCOMM Comput. Commun. Rev.* 44, 4 (Aug. 2014), 619–630. doi:10.1145/2740070.2626312

[70] Yao Peng, Longfei Shangguan, Yue Hu, Yujie Qian, Xianshang Lin, Xiaojiang Chen, Dingyi Fang, and Kyle Jamieson. 2018. PLoRa: a passive long-range data network from ambient LoRa transmissions. In *Proceedings of the 2018 Conference of the ACM Special Interest Group on Data Communication* (Budapest, Hungary) *(SIGCOMM '18)*. Association for Computing Machinery, New York, NY, USA, 147–160. doi:10.1145/3230543.3230567

[71] Carlos Pérez-Penichet, Frederik Hermans, Ambuj Varshney, and Thiemo Voigt. 2016. Augmenting IoT networks with backscatter-enabled passive sensor tags. In *Proceedings of the 3rd Workshop on Hot Topics in Wireless* (New York City, New York) *(HotWireless '16)*. Association for Computing Machinery, New York, NY, USA, 23–27. doi:10.1145/2980115.2980132

[72] A. Pohl. 2000. A review of wireless SAW sensors. *IEEE Transactions on Ultrasonics, Ferroelectrics, and Frequency Control* 47, 2 (2000), 317–332. doi:10.1109/58.827416

[73] NPP Pulsar. 2023. *3I306E Gallium Arsenide Tunnel Diode Technical Specifications*. USSR Ministry of Electronic Industry. http://w140.com/tekwiki/wiki/Russian_tunnel_diodes [Accessed: 2025-08-10].

[74] Carlos Pérez-Penichet, Claro Noda, Ambuj Varshney, and Thiemo Voigt. 2018. Battery-Free 802.15.4 Receiver. In *2018 17th ACM/IEEE International Conference on Information Processing in Sensor Networks (IPSN)*. 164–175. doi:10.1109/IPSN.2018.00045

[75] Lord Rayleigh. 1885. On waves propagated along the plane surface of an elastic solid. *Proceedings of the London mathematical Society* 1, 1 (1885), 4–11.

[76] C. Rajashekar Reddy, Manoj Gulati, and Ambuj Varshney. 2023. Beyond Broadcasting: Revisiting FM Frequency-band for Providing Connectivity to Next Billion Devices. In *Proceedings of the 11th International Workshop on Energy Harvesting & Energy-Neutral Sensing Systems* (Istanbul, Turkiye) *(ENSsys '23)*. Association for Computing Machinery, New York, NY, USA, 30–36. doi:10.1145/3628353.3628546

[77] C. Rajashekar Reddy, Dhairya J. Shah, Nobel Ang, and Ambuj Varshney. 2025. AudioCast: Enabling Ubiquitous Connectivity for Embedded Systems. *Proc. ACM Interact. Mob. Wearable Ubiquitous Technol.* 9, 2, Article 27 (2025), 32 pages. doi:10.1145/3729471

[78] Mohammad Rostami, Xingda Chen, Yuda Feng, Karthikeyan Sundaresan, and Deepak Ganesan. 2021. MIXIQ: Re-Thinking Ultra-Low Power Receiver Design for next-Generation on-Body Applications. In *Proceedings of the 27th Annual International Conference on Mobile Computing and Networking* (New Orleans, Louisiana) *(MobiCom '21)*. Association for Computing Machinery, New York, NY, USA, 364–377.

[79] Jihoon Ryoo, Yasha Karimi, Akshay Athalye, Milutin Stanaćević, Samir R. Das, and Petar Djurić. 2018. BARNET: Towards Activity Recognition Using Passive Backscattering Tag-to-Tag Network. In *Proceedings of the 16th Annual International Conference on Mobile Systems, Applications, and Services* (Munich, Germany) *(MobiSys '18)*. Association for Computing Machinery, New York, NY, USA, 414–427. doi:10.1145/3210240.3210336

[80] M. B. Schulz, B. J. Matsinger, and M. G. Holland. 1970. Temperature Dependence of Surface Acoustic Wave Velocity on α Quartz. *J. Appl. Phys.* 41, 7 (1970), 2755–2765. doi:10.1063/1.1659315

[81] RCA Corporation. Semiconductor and Materials Division. 1963. *RCA Tunnel Diode Manual*. RCA. [Accessed: 2025-11-20].

[82] Linbo Shao, Mingji Yu, Smarak Maity, Neil Sinclair, Lu Zheng, Cindy Chia, Amirhassan Shams-Ansari, Cheng Wang, Mian Zhang, Keji Lai, and Marko Lončar. 2019. Microwave-to-Optical Conversion Using Lithium Niobate Thin-Film Acoustic Resonators. *Optica* 6, 12 (2019), 1498–1505. doi:10.1364/OPTICA.6.001498

[83] William R. Shreve and Robert E. Stigall. 2007. Surface Acoustic Wave Devices for Use in a High Performance Television Tuner. *IEEE Transactions on Consumer Electronics* 1 (2007), 96–104.

[84] Signal Hound. 2023. BB60D 6 GHz Spectrum Analyzer. Data Sheet. https://signalhound.com/sigdownloads/datasheets/Signal-Hound-BB60D-Data-Sheet.pdf [Accessed: 2025-11-20].

[85] H. S. Sommers, Jr. 1959. Tunnel Diodes as High-Frequency Devices. *Proceedings of the IRE* 47, 7 (July 1959), 1201–1206. doi:10.1109/JRPROC.1959.287467

[86] Yihang Song, Li Lu, Jiliang Wang, Chong Zhang, Hui Zheng, Shen Yang, Jinsong Han, and Jian Li. 2023. Mote: Enabling Passive Chirp De-spreading and W-level Long-Range Downlink for Backscatter Devices. In *20th USENIX Symposium on Networked Systems Design and Implementation (NSDI 23)*. USENIX Association, Boston, MA, 1751–1766.

[87] F. Sterzer and D. E. Nelson. 1961. Tunnel-Diode Microwave Oscillators. *Proceedings of the IRE* 49, 4 (April 1961), 744–753. doi:10.1109/JRPROC.1961.287850

[88] Syrlinks. 2020. EWOS10/20: Ultra-Low Power OCXO for Mil/Aero/General Industry. https://safran-navigation-timing.com/wp-content/uploads/2023/02/EWOS10-20.pdf Datasheet, Version 1.0, updated August 26, 2020, [Accessed: 2026-03-30].

[89] Syrlinks. 2021. EWOS16-UW: Ultra-Low Power micro-OCXO for Underwater Systems. https://safran-navigation-timing.com/wp-content/uploads/2023/02/EWOS16-UW-29102021.pdf Datasheet, Version 1.1, updated October 29, 2021, [Accessed: 2026-03-30].

[90] TAI-SAW Technology Co., Ltd. 2014. *TC0219C Rev. 6.0: SAW Resonator 433.92 MHz*. https://www.taisaw.com/assets/PDF/TC0219C%20_Rev.6.0_.pdf [Accessed: 2025-11-20].

[91] Vamsi Talla, Mehrdad Hessar, Bryce Kellogg, Ali Najafi, Joshua R. Smith, and Shyamnath Gollakota. 2017. LoRa Backscatter: Enabling The Vision of Ubiquitous Connectivity. *Proc. ACM Interact. Mob. Wearable Ubiquitous Technol.* 1, 3, Article 105 (Sept. 2017), 24 pages. doi:10.1145/3130970

[92] Vamsi Talla, Bryce Kellogg, Shyamnath Gollakota, and Joshua R. Smith. 2017. Battery-Free Cellphone. *Proc. ACM Interact. Mob. Wearable Ubiquitous Technol.* 1, 2, Article 25 (June 2017), 20 pages. doi:10.1145/3090090

[93] Vamsi Talla, Joshua Smith, and Shyamnath Gollakota. 2021. Advances and Open Problems in Backscatter Networking. *GetMobile: Mobile Comp. and Comm.* 24, 4 (March 2021), 32–38. doi:10.1145/3457356.3457367

[94] Vamsi Talla and Joshua R Smith. 2013. Hybrid analog-digital backscatter: A new approach for battery-free sensing. In *2013 IEEE international conference on RFID (RFID)*. IEEE, 74–81. doi:10.1109/RFID.2013.6548138

[95] Texas Instruments. 2023. CC1310: SimpleLink™ Ultra-Low-Power Sub-1 GHz Wireless MCU. Datasheet SWRS181D. https://www.ti.com/lit/ds/symlink/cc1310.pdf [Accessed: 2025-11-20].

[96] Lim Chang Quan Thaddeus, C. Rajashekar Reddy, Yuvraj Singh Bhadauria, Dhairya Shah, Manoj Gulati, and Ambuj Varshney. 2024. TunnelSense: Low-Power, Non-Contact Sensing Using Tunnel Diodes. In *2024 IEEE International Conference on RFID (RFID)*. 154–159. doi:10.1109/RFID62091.2024.10582671

[97] Tijs van Dam and Koen Langendoen. 2003. An adaptive energy-efficient MAC protocol for wireless sensor networks. In *Proceedings of the 1st International Conference on Embedded Networked Sensor Systems* (Los Angeles, California, USA) *(SenSys '03)*. Association for Computing Machinery, New York, NY, USA, 171–180. doi:10.1145/958491.958512

[98] Craig T. Van Degrift. 1975. Tunnel Diode Oscillator for 0.001 ppm Measurements at Low Temperatures. *Rev. Sci. Instrum.* 46, 5 (1975), 599–607. doi:10.1063/1.1134272

[99] Ambuj Varshney and Lorenzo Corneo. 2020. Tunnel Emitter: Tunnel Diode Based Low-Power Carrier Emitters for Backscatter Tags. In *Proceedings of the 26th Annual International Conference on Mobile Computing and Networking* (London, United Kingdom) *(MobiCom '20)*. Association for Computing Machinery, New York, NY, USA, Article 42, 14 pages. doi:10.1145/3372224.3419199

[100] Ambuj Varshney, Oliver Harms, Carlos Pérez-Penichet, Christian Rohner, Frederik Hermans, and Thiemo Voigt. 2017. LoRea: A Backscatter Architecture That Achieves a Long Communication Range. In *Proceedings of the 15th ACM Conference on Embedded Network Sensor Systems* (Delft, Netherlands) *(SenSys '17)*. Association for Computing Machinery, New York, NY, USA, Article 18, 14 pages. doi:10.1145/3131672.3131691

[101] Ambuj Varshney, Carlos Pérez Penichet, Christian Rohner, and Thiemo Voigt. 2017. Towards Wide-area Backscatter Networks. In *Proceedings of the 4th ACM Workshop on Hot Topics in Wireless* (Snowbird, Utah, USA) *(HotWireless '17)*. Association for Computing Machinery, New York, NY, USA, 49–53. doi:10.1145/3127882.3127888

[102] Ambuj Varshney, Andreas Soleiman, Luca Mottola, and Thiemo Voigt. 2017. Battery-free Visible Light Sensing. In *Proceedings of the 4th ACM Workshop on Visible Light Communication Systems* (Snowbird, Utah, USA) *(VLCS '17)*. Association for Computing Machinery, New York, NY, USA, 3–8. doi:10.1145/3129881.3129890

[103] Ambuj Varshney, Andreas Soleiman, and Thiemo Voigt. 2019. TunnelScatter: Low Power Communication for Sensor Tags Using Tunnel Diodes. In *The 25th Annual International Conference on Mobile Computing and Networking* (Los Cabos, Mexico) *(MobiCom '19)*. Association for Computing Machinery, New York, NY, USA, Article 50, 17 pages. doi:10.1145/3300061.3345451

[104] Ambuj Varshney, Wenqing Yan, and Prabal Dutta. 2022. Judo: Addressing the Energy Asymmetry of Wireless Embedded Systems through Tunnel Diode Based Wireless Transmitters. In *Proceedings of the 20th Annual International Conference on Mobile Systems, Applications and Services* (Portland, Oregon) *(MobiSys '22)*. Association for Computing Machinery, New York, NY, USA, 273–286. doi:10.1145/3498361.3538923

[105] Han Wang, Yihang Song, Qianhe Meng, Zetao Gao, Chong Zhang, and Li Lu. 2024. Sisyphus: Redefining Low Power for LoRa Receiver. In *Proceedings of the 30th Annual International Conference on Mobile Computing and Networking* (Washington D.C., DC, USA) *(ACM MobiCom '24)*. Association for Computing Machinery, New York, NY, USA, 1177–1191. doi:10.1145/3636534.3690686

[106] Ju Wang, Omid Abari, and Srinivasan Keshav. 2018. Challenge: RFID Hacking for Fun and Profit. In *Proceedings of the 24th Annual International Conference on Mobile Computing and Networking* (New Delhi, India) *(MobiCom '18)*. Association for Computing Machinery, New York, NY, USA, 461–470. doi:10.1145/3241539.3241561

[107] Shih-Hsing Wang and Chung-Chih Hung. 2019. A 0.35-V 240-W Fast-Lock and Low-Phase-Noise Frequency Synthesizer for Implantable Biomedical Applications. *IEEE Transactions on Biomedical Circuits and Systems* 13, 6 (2019), 1759–1770. doi:10.1109/TBCAS.2019.2941090

[108] Roy Want. 2006. An introduction to RFID technology. *IEEE Pervasive Computing* 5, 1 (2006), 25–33. doi:10.1109/MPRV.2006.2

[109] Robert L. Watters. 1963. Negative Resistance Diode Oscillator. U.S. Patent. https://patents.google.com/patent/US3081436A/en US Patent 3,081,436.

[110] G. Werner-Allen, J. Johnson, M. Ruiz, J. Lees, and M. Welsh. 2005. Monitoring volcanic eruptions with a wireless sensor network. In *Proceedings of the Second European Workshop on Wireless Sensor Networks, 2005.* 108–120. doi:10.1109/EWSN.2005.1462003

[111] Brad Wheeler, Filip Maksimovic, Nima Baniasadi, Sahar Mesri, Osama Khan, David Burnett, Ali Niknejad, and Kris Pister. 2017. Crystal-free narrow-band radios for low-cost IoT. In *2017 IEEE Radio Frequency Integrated Circuits Symposium (RFIC)*. 228–231. doi:10.1109/RFIC.2017.7969059

[112] Richard M. White and Fred W. Voltmer. 1965. Direct piezoelectric coupling to surface elastic waves. *Applied physics letters* 7, 12 (1965), 314–316.

[113] Zonglin Wu, Yubo Zhang, Shuxian Wu, Hangyu Qian, Feihong Bao, Xiongchuan Huang, Jie Zou, and Guo-Min Yang. 2025. Ultralow-Power Consumption High FoM Digitally Controlled Tunable Oscillator Utilizing SH-SAW Resonator Based on 4H-SiC Substrate. *IEEE Transactions on Electron Devices* 72, 9 (2025), 5130–5137. doi:10.1109/TED.2025.3586234

[114] Kai Xu, Wei Gong, Yuepei Li, Jayakrishnan Methapettyparambu Purushothama, George Goussetis, Stephen McLaughlin, John S. Thompson, Chaoyun Song, and Yuan Ding. 2024. FM Rider: Two-FSK Modulation-Based Ambient FM Backscatter Over 100 m Distance. *IEEE Transactions on Microwave Theory and Techniques* 72, 9 (2024), 5563–5575. doi:10.1109/TMTT.2024.3367439

[115] Y. Yasuhara, N. Yamaji, T. Kurokawa, and K. Takahashi. 1982. Surface Acoustic Wave Devices for Consumer Use. *IEEE Transactions on Consumer Electronics* CE-28, 3 (1982), 475–481. doi:10.1109/TCE.1982.353946

[116] D. T. Young, C. A. Burrus, and R. C. Shaw. 1964. High Efficiency Millimeter-Wave Tunnel-Diode Oscillators. *Proc. IEEE* 52, 10 (Oct. 1964), 1260–1261. doi:10.1109/PROC.1964.3346 Correspondence.

[117] Z-Communications, Inc. 2026. *USSP2400-LF: 2400–2485 MHz Voltage-Controlled Oscillator (Surface-Mount Module), Rev A1*. Z-Communications, Inc., Poway, CA. https://zcomm.com/datasheets/VCO-datasheets/USSP2400-LF.pdf Datasheet, Rev A1; [Accessed: 2025-11-20].

[118] Maolin Zhang, Si Chen, Jia Zhao, and Wei Gong. 2021. Commodity-level BLE backscatter. In *Proceedings of the 19th Annual International Conference on Mobile Systems, Applications, and Services* (Virtual Event, Wisconsin) *(MobiSys '21)*. Association for Computing Machinery, New York, NY, USA, 402–414. doi:10.1145/3458864.3466865

[119] Pengyu Zhang, Dinesh Bharadia, Kiran Joshi, and Sachin Katti. 2016. HitchHike: Practical Backscatter Using Commodity WiFi. In *Proceedings of the 14th ACM Conference on Embedded Network Sensor Systems* (Stanford, CA, USA) *(SenSys '16)*. Association for Computing Machinery, New York, NY, USA, 259–271. doi:10.1145/2994551.2994565

[120] Pengyu Zhang, Pan Hu, Vijay Pasikanti, and Deepak Ganesan. 2015. EkhoNet: High-Speed Ultra Low-Power Backscatter for Next Generation Sensors. *GetMobile: Mobile Comp. and Comm.* 19, 2 (Aug. 2015), 14–17. doi:10.1145/2817761.2817766

[121] Yubo Zhang, Zonglin Wu, Suhao Cherr, Mingke Cherr, Feihong Bao, Jie Zou, and Xiongchuan Huang. 2024. A 984MHz 123W Ultra-Low-Power Digitally Controlled Oscillator Based on SiC SAW Resonator with 221dBc/Hz FoM. In *2024 International Conference on Microwave and Millimeter Wave Technology (ICMMT)*, Vol. 1. 1–3. doi:10.1109/ICMMT61774.2024.10672477

[122] Renjie Zhao, Kejia Wang, Kai Zheng, Xinyu Zhang, and Vincent Leung. 2023. SlimWiFi: Ultra-Low-Power IoT Radio Architecture Enabled by Asymmetric Communication. In *20th USENIX Symposium on Networked Systems Design and Implementation (NSDI 23)*. USENIX Association, Boston, MA, 1201–1219.

[123] Fengyuan Zhu, Luwei Feng, Meng Jin, Xiaohua Tian, Xinbing Wang, and Chenghu Zhou. 2023. Towards Ultra-Low Power OFDMA Downlink Demodulation. In *Proceedings of the 20th ACM Conference on Embedded Networked Sensor Systems* (Boston, Massachusetts) *(SenSys '22)*. Association for Computing Machinery, New York, NY, USA, 725–739. doi:10.1145/3560905.3568509

[124] Fengyuan Zhu, Mingwei Ouyang, Luwei Feng, Yaoyu Liu, Xiaohua Tian, Meng Jin, Dongyao Chen, and Xinbing Wang. 2022. Enabling software-defined PHY for backscatter networks. In *Proceedings of the 20th Annual International Conference on Mobile Systems, Applications and Services* (Portland, Oregon) *(MobiSys '22)*. Association for Computing Machinery, New York, NY, USA, 330–342. doi:10.1145/3498361.3538927

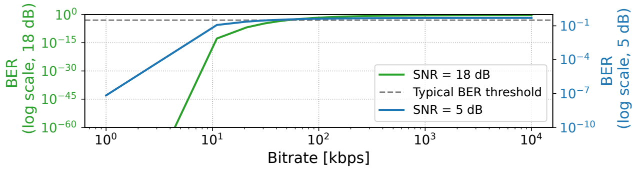

Figure 24: BER for 2-FSK modulation is estimated from measured IF SNR values and supported bitrate.

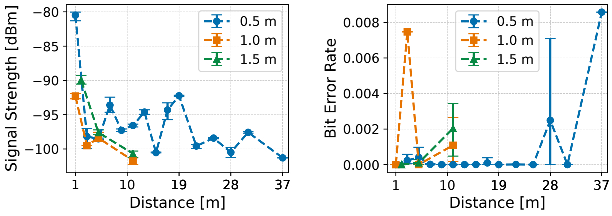

(a) RSSI with Varying Distance (b) BER with Varying Distance

Figure 25: M² operates as a carrier emitter for backscatter communication. As the ED to tag separation increases, both the backscattered signal strength and the communication range decreases.

A Comparison of State-of-the-art Oscillators

Modern wireless embedded systems employ a mix of ring, LC/DCO, resonator-referenced, and precision-reference oscillators, which are increasingly integrated into full transceiver chips rather than exposed as standalone blocks. For example, crystal-free narrowband radios often share an LC-tank digitally controlled oscillator across RX and TX to reduce power and area [6, 7], but still rely on over-the-air references and careful calibration to remain on-channel. At the other extreme, free-running ring-oscillator systems can achieve low power but typically require receiver-side drift compensation or protocol support to remain decodable. Precision references such as OCXOs occupy the opposite end of the design space. They offer excellent frequency stability and low phase noise, but are generally used as low-frequency references and require an additional PLL synthesis chain to generate an RF carrier at the target band.

Across these oscillator families, three challenges recur. *(i) Frequency stability (ppm):* free-running rings without a crystal can support packet-level communication only with receiver assistance or over-the-air correction; absolute ppm-level stability is generally unavailable without a reference [53, 111]. SAW and crystal-referenced designs improve this significantly, while OCXOs push stability further, albeit typically as reference sources rather than direct RF oscillators. *(ii) Phase-noise versus power tradeoff:* LC oscillators improve close-in phase noise but usually at the cost of higher current and larger area; commercial VCOs offer good phase noise while consuming a few milliwatts, which is often too costly for small-battery or battery-free nodes [55–57]. OCXOs can achieve excellent spectral purity, but their tens-of-milliwatts power cost and need for a synthesizer chain make them unsuitable for low-power RF designs. *(iii) Temperature drift, aging, and supply sensitivity:* SAW-resonator oscillators provide tight initial tolerance and low temperature coefficients using simple single-transistor loops, but are typically fixed-frequency, have limited pulling range, and offer modest RF output, making them well suited to beacon-class nodes [28, 62, 113, 121]. M² targets this operating point but at substantially lower power than conventional RF oscillators.

M² co-designs an RTO such that the high-Q resonator anchors the carrier, while the tunnel diode's SoM behavior collapses what would otherwise be separate LO and mixer stages into a single stage. Unlike prior TDO based transmitters such as Judo [104] that require injection locking to an external carrier signal from ED for stability, or TDO designs that retain low power by tolerating much poorer stability [65, 77, 99], M² preserves microwatt-class TDO operation while removing the ED by allowing the resonator to define the oscillation frequency. In this sense, M² bridges the gap between discrete low-power SAW oscillators and integrated LC or ring-based radios, yielding a standalone low-power RF carrier source with practical stability and phase noise for sub-GHz applications. Table 5 summarizes related systems and commercial oscillators.

B Estimated BER from Measured SNR

We estimate the achievable bitrate of the M² receiver from the measured SNR of the downconverted IF signal using standard BER expressions for 2-FSK modulation [54]. We use representative measured SNR values of 18 dB and 5 dB, corresponding to NLoS locations L1 and L12, respectively. For each case, we convert the measured SNR to an effective E_b/N_0 as a function of bitrate and compute the corresponding BER. Figure 24 shows the resulting analytical estimate and the 10^{-3} BER threshold. The results suggest that the M² receiver can support bitrates exceeding 10 kbps in this complex NLoS environment. We emphasize that this is an SNR-based estimate derived from measured downconverted signal quality, rather than a BER measurement of a complete receiver.

C M² as an Emitter Device for Backscatter

M² can also function as an ED that provides the carrier for backscatter communication. To evaluate this, we place M² as an ED at a fixed location in a LoS environment and position a legacy backscatter tag at fixed ED to backscatter tag separations of 0.5 m, 1.0 m, and 1.5 m. We then vary the distance between the tag and the receiver to study both signal strength and link reliability. For the signal-strength experiment, the backscatter tag is configured with a baseband tone at 100 kHz, and the strength of the backscattered signal is measured using a spectrum analyzer. Figure 25(a) shows that the received backscattered signal decreases as the receiver distance increases and as the ED to tag separation grows, as expected. For the reliability experiment, the backscatter tag is configured for 2-FSK modulation at 3 kbps, following the same packet structure as earlier experiments, and the backscattered packets are decoded using the same receiver setup as in the main evaluation. Figure 25(b) shows that when the ED to tag separation is 0.5 m, the system supports backscatter communication up to 37 m while maintaining BER below 0.01. When the ED to tag separation is increased to 1.0 m and 1.5 m, communication remains reliable up to about 11 m, again with BER below 0.01. These results suggest that M² can serve as a practical low-power ED for backscatter tags.

D RTO using Tunnel Diode 3I306E

We build an RTO in the 433 MHz band using the 3I306E tunnel diode and evaluate its frequency and amplitude stability over 4 hours, as reported in Table 3. Its I-V characteristics are shown in Figure 3. Figure 26 shows the drift over this period. As shown in Table 3,

System / Work	**Frequency band**	**Stability**	**Phase noise**	**Power consumption**	**RF strength**
Kim et al. (2016) [45]	400 MHz	N/R	−90.3 dBc/Hz @ 1 MHz	242.1 µW*	N/R
Wheeler et al. (2017) [111]	2.6-3.1 GHz	40 ppm	−92.1 dBc/Hz @ 100 kHz	1.537 mW*	−5.3 dBm
Burnett et al. (2017) [7]	2.4 GHz	$\sigma_f \approx 491$ kHz	N/R	105 µW*	N/R
Jung et al. (2018) [40]	490 MHz	N/R	−94.84 dBc/Hz @ 1 MHz	45 µW*	N/R
Maksimovic et al. (2019) [53]	2.4 GHz	40 ppm	N/R	847 µW*†	−10 dBm
Wang et al. (2019) [107]	400-433 MHz	N/R	−105.65 dBc/Hz @ 1 MHz	240 µW*	−20 dBm
Varshney et al. (2019) [103][1]	868 MHz	N/R	≈ −80 dBc/Hz[2] @ 100 kHz	57 µW	−19 dBm
Burnett et al. (2020) [6]	2.4 GHz	$\sigma = 677$ kHz	N/R	105 µW* RX; 364 µW* TX	−12 dBm‡
Lin et al. (2021) [49]	921.6 MHz	N/R	−96.2 dBc/Hz @ 1 MHz	287.35 µW*	−14 dBm
Cheng et al. (2023) [10]	423-450 MHz	N/R	−88 dBc/Hz @ 1MHz	870 µW	−7 dBm*†
Chang et al. (2024) [8]	419-445 MHz	N/R	−87 dBc/Hz @ 1 MHz	890 µW*†	−6.9 dBm
Wu et al. (2025) [113, 121][3]	984 MHz	17.2 ppm/°C	−125.9 dBc/Hz @ 100 kHz	123 µW*	N/R
MAX2608 [56]	300−500 MHz	N/R	−100 dBc/Hz @ 100 kHz	7.425 mW	−10 dBm
USSP2400−LF [117]	2.4 GHz	N/R	−83 dBc/Hz @ 10 kHz	16.2 mW	−1.5 dBm
MAX2622 [57]	855−881 MHz	N/R	−101 dBc/Hz @ 100 kHz	24 mW @ 3 V	−3 dBm
MAX2750 [55]	2400−2500 MHz	N/R	−125 dBc/Hz @ 4 MHz	34 mW @ 3 V	−3 dBm
SARCC433M92BXM0[4] [62]	433.92 MHz	N/R	N/R	≈12 mW[2]	≈-30 dBm[2]
EPCOS R727 QCC8C[5] [28]	433.92 MHz	N/R	N/R	10.5 mW[2]	−20 dBm
EWOS16-UW[6] [89]	16.384 MHz	0.05 ppm	−148 dBc/Hz @ 10 kHz	50 mW	N/R
EWOS10/20[6] [88]	10/20 MHz	0.10 ppm	−150 dBc/Hz @ 10 kHz	75 mW	N/R
This work (2025)	**433 MHz**	2.1 ppm	-92.25 dBc/Hz @ 10 kHz, -119.02 dBc/Hz @ 1 MHz	105 µW	−17.5 dBm

N/R: Not reported *Values reported for ASIC implementations †Includes oscillator and PA ‡ After using PA that consumes 1.6 mW [1]Tunnel diode-based oscillator [2]Estimated value from spectrum; exact value not reported [3]Uses SiC SAW resonator [4]Application notes give a design using a 2SC4228 (NEC) transistor [5]433.92 MHz Colpitts topology using BFR92P (Infineon) transistor [6]OCXO reference oscillator; generating an RF carrier at the target frequency requires an additional PLL.

Table 5: Performance comparison of low-power RF oscillators and selected low-power reference oscillators (OCXOs). Research prototypes appear above the first midrule; commercial direct-RF oscillators appear below it; OCXO reference sources are shown separately because they are not direct RF carriers.

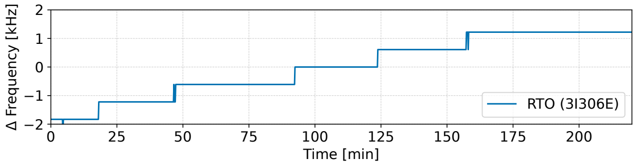

Figure 26: An RTO built with the 3I306E tunnel diode exhibits peak-to-peak frequency drift of about 3.05 kHz **over 4 hours of continuous operation.**

we observe a stability of 5.62 ppm and an amplitude deviation of 0.069 dB. This further suggests that M² is scalable across tunnel diode types and is not limited to a specific variant.

E Comparison of Transmitter and Receiver Architectures

Figure 27 places M² in the context of prior transmitter and receiver architectures. Existing designs typically achieve low power by delegating part of the radio functionality to external infrastructure, such as a nearby ED, helper tone, or external local oscillator. While these approaches reduce the energy cost at the tag, they require additional infrastructure, limit range, or restrict supported modulation schemes, ultimately constraining deployment scenarios.

Transmitter architectures. Backscatter transmitters [50, 91, 100, 119], as shown in Figure 27(a), communicate by reflecting and modulating an external carrier generated by a nearby ED. This enables low tag power, but the link depends on the availability and strength of the external carrier, which limits range and deployment flexibility. Reflection-amplifier backscatter transmitters [2, 17], shown in Figure 27(c), partially address this limitation by amplifying the reflected signal, but they still require an ED and introduce stronger unwanted harmonics. Injection-locked transmitters [104], shown in Figure 27(e), can achieve longer range by stabilizing the TDO through injection-locking with an external carrier signal, but they continue to rely on an ED. In contrast, as shown in Figure 27(g), M² generates its own stable carrier signal locally while retaining microwatt-scale operation, removing the need for a dedicated ED.

Receiver architectures. Envelope-detector receivers [50, 69, 94], shown in Figure 27(b), offer low-power reception, but their sensitivity is limited and they are restricted to simple modulation schemes. External-local-oscillator receivers [19, 74, 78, 86], shown in Figure 27(d), support downconversion but require a separate helper tone or externally generated LO, which again shifts complexity to infrastructure like an ED. Injection-locked receivers [58], shown in Figure 27(f), use an external carrier to stabilize the TDO during reception, but remain dependent on an ED. In contrast, as shown in Figure 27(h), M² in receive mode downconverts via autodyning using its own SAW-stabilized oscillator, enabling a standalone low-power frontend without requiring a dedicated ED for stability.

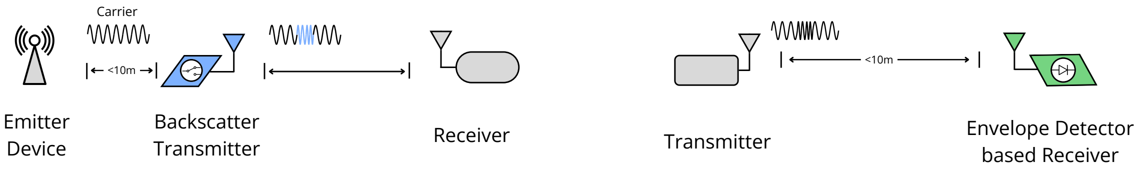

(a) Backscatter Transmitter (b) Envelope Detector based Receiver

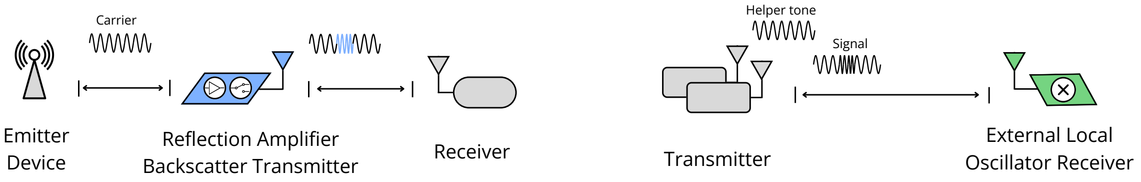

(c) Reflection Amplifier Backscatter Transmitter (d) External Local Oscillator Receiver

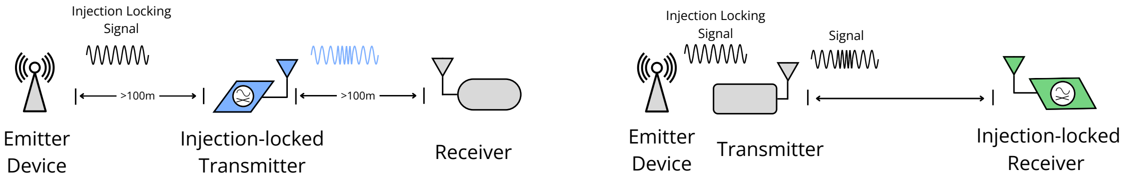

(e) Injection-locked Transmitter (f) Injection-locked Receiver

(g) M² as Transmitter (h) M² as Receiver

Figure 27: ***Prior transmitter architectures:*** **(a) Backscatter transmitters reflect an external carrier, requiring a nearby ED and limiting range. (c) Reflection-amplifier backscatter transmitters amplify the reflected signal but still depend on an ED and can generate stronger harmonics. (e) Injection-locked transmitters improve stability but still rely on an ED.** ***Prior receiver architectures:*** **(b) Envelope-detector receivers are low power but offer limited sensitivity and support only simple modulation. (d) External-local-oscillator receivers support general downconversion but require a separate ED. (f) Injection-locked receivers depend on an ED. (g, h) M² enables both transmission and reception using its own SAW-stabilized oscillator, eliminating the need for a dedicated ED.**